UTRECHT UNIVERSITY

MSC THESIS

Examining the effect of fluid flow on the stress and strain evolution of Dutch geothermal reservoirs and the implications for induced seismicity

Author:
Lynn VOGEL

Supervisors:
Dr. Ylona VAN DINTHER
Dr. Fred Beekman

A thesis submitted in fulfillment of the requirements for the degree of Master of Science in

Earth Structure and Dynamics

June 7, 2023

Universiteit Utrecht

UTRECHT UNIVERSITY

Abstract

Geosciences
Earth Structure and Dynamics

Master of Science

Examining the effect of fluid flow on the stress and strain evolution of Dutch geothermal reservoirs and the implications for induced seismicity

by Lynn VOGEL

Geothermal energy is expected to produce 23% of the total heat demand in the Netherlands by 2050. As geothermal energy production is known to induce seismicity, risk assessment is crucial for a safe transition to new energy sources. The exact mechanisms inducing seismicity in geothermal reservoirs are, however, very complex and poorly understood.

In this thesis, a fully coupled seismo-hydro-mechanical numerical code by Petrini (2019) is adapted to work for a geothermal setting with a set-up that represents the Dutch subsurface. The main goal is to investigate whether this code is suited for studying such a setting and to debug any potential mistakes in the code. Furthermore, the aim is to investigate how stress and strain build-up due to geothermal energy production in the Dutch subsurface. Lastly, a parameter study is executed to examine the effect of operational parameters (injection and production rates) and fault material parameters.

The adapted code successfully triggers multiple (seismic) events, giving insight into the relationship between fluid flow and solid deformation during multiple phases: 1) inter-seismic, 2) nucleation, 3) propagation, and 4) post-seismic. The seismicity that was triggered, however, was very mild (M_L<2.0), meaning that it would not be felt at the surface.

While the code is very efficient in examining the short-term effects (i.e. less than a year) of geothermal energy production, it requires too much computational time to see what happens if geothermal energy were to be produced long-term (i.e. for decades of production). Insights are offered into why the computational time is so long and solutions are offered for future work.

Contents

List of Figures

List of Tables

List of Symbols

symbol	parameter	variations	unit
σ'_{ij}	deviatoric stress		Pa
σ_{II}	second invariant of the deviatoric stress		Pa
$\frac{D\sigma'_{ij}}{\widehat{Dt}}$	co-rotational time derivative of the deviatoric stress component		Pa/s
σ_{yield}	yield strength		Pa
$\dot{\varepsilon}_{ij}$	strain rate		s^{-1}
$\dot{\varepsilon}'_{ij}$	deviatoric strain rate		s^{-1}
$\dot{\varepsilon}'_{II}$	second invariant of the deviatoric strain rate		s^{-1}
p	pressure	t: total f: fluid s: solid	Pa
ν	velocity	D: Darcy f: fluid s: solid	m/s
g	gravitational acceleration		m/s^2
φ	connected porosity		
K	bulk modulus	s: solid d: drained φ: of pores	Pa
μ	shear modulus	φ: effective 0: solid rock grain	Pa
k^{φ}	permeability	r: reference permeability	
ρ	density	t: total f: fluid s: solid	kg/m^3
η	viscosity	φ: effective f: fluid s: solid 0: solid rock grain	Pa·s
α	Biot-Willis coefficient		
β	Skempton's coefficient		
$G_{plastic}$	plastic flow potential		Pa
χ	plastic multiplier		s^{-1}
Z	visco-elasticity factor		
$\frac{D}{Dt}$	Lagrangian time derivative	s: solid f: fluid	

Chapter 1

Introduction

The Netherlands is due to reduce carbon emissions by 95% by 2050 (with respect to 2015) (Stichting Platform Geothermie (2018)). This goal is only obtainable by relying heavily on renewable energy sources, such as geothermal energy. In 2015 0.3% of the total energy and heat consumption in the Netherlands came from geothermal sources (used mainly for horticultural purposes): this is expected to rise to 5% in 2030 and 23% in 2050 (Stichting Platform Geothermie (2018)). To ensure a successful and safe energy transition, it is of utmost importance to assess the potential hazards related to (long-term) geothermal energy production.

A potential and concerning hazard is induced seismic events (i.e. earthquakes due to human activities). In the Netherlands geothermal energy is mainly produced with the use of two wells (i.e. a doublet): an injection and a production well. The injection of fluids (e.g. Li et al. (2019) and Rathnaweera et al. (2020)) into a reservoir and the depletion of fluids and gasses (e.g. Buijze et al. (2017)) from the subsurface have both been known to trigger earthquakes. Seismic hazards should therefore be assessed in great detail, as geothermal systems involve a combination of withdrawal and injection. However, the driving mechanisms for triggering earthquakes related to the extraction and injection of fluids are not fully understood.

The potential for felt, induced seismicity (M>2.0) in geothermal systems is examined in Buijze et al. (2019). Herein is stated that due to reservoir properties (e.g. large distance to crystalline basement) and operational parameters (e.g. no net volume change) Dutch geothermal systems targeting the Upper Jurassic and Lower Cretaceous sandstones are not likely to induce felt seismicity (Buijze et al. (2019)). There is more uncertainty surrounding the Slochteren Formation- which is also the targeted formation for gas depletion in the Groningen gas fields- as an aquifer for geothermal operations (Buijze et al. (2019)). Gas depletion has led to induced seismicity within the reservoir and even though the pressure changes involved with geothermal energy production are smaller than those related to gas extraction, the author suggests that thermo-elastic stressing may be large (Buijze et al. (2019)). Buijze et al. (2019) is cautiously optimistic about the future of geothermal energy in the Netherlands. Suggesting that the risk for felt induced seismicity is low for the main targeted formations while acknowledging that the occurrence of induced seismicity depends on many factors specific to a certain site and should always be taken into consideration.

It is important to note that the focus of Buijze et al. (2019) lies on the occurrence of felt seismicity and no attention is paid to the frequency of seismicity. The induced seismicity in the Groningen gas field was often not larger than M = 2.0. Nevertheless these earthquakes are considered a great nuisance as they have caused considerable damage to homes. The possibility of smaller seismic events should therefore not be neglected in hazard assessments for geothermal operations in the Netherlands.

The relationship between fluid flow and solid deformation has been studied in previous studies (e.g. Li et al. (2019), Rathnaweera et al. (2020), Yarushina et

al. (2015) and Petrini et al. (2020)). Petrini et al. (2020) presents a seismo-hydro-mechanical numerical model of a subduction zone in which fluid flow and solid deformation are fully coupled based on Biot's poro-elasticity theory (Biot (1941), Biot (1955), Biot (1956a), and Biot (1956b)). The modeled results emphasize the crucial role fluid flow can encompass in a subduction zone. The strength of the fault rock can vary based solely on the coupling between the solid matrix and the fluid it bears, without incorporating a rate- or rate- and state-dependent friction (e.g. van Dinther et al. (2013)), resulting in full seismic cycles and the simulation of both regular earthquakes and slower events (Petrini et al. (2020)). The slip behavior was found to be controlled by the rock permeability: the highest tested rock permeability of (1e-19m^2) led to megathrusts, while the lowest tested permeability (3e-20m^2) led to stable aseismic slip (Petrini et al. (2020)).

The current study offers an adaptation of the model presented by Petrini et al. (2020), further examining the role of solid-fluid coupling, however, now focused on geothermal energy production in the Netherlands. The main objective of this study is to assess whether the model is suited for examining a geothermal setting. A secondary task herein is to debug the code for any mistakes that may exist. A simple geothermal set-up is used (based on the model used in van Wees et al. (2020)) to examine the role of solid-fluid coupling on the stress and strain within a typical Dutch, geothermal reservoir. Finally, a parameter study is conducted, examining the effects of: injection and extraction pressure rates, fault offset, fault permeability, fault porosity, and fault strength.

Chapter 2 presents background information on the classification of Dutch, geothermal reservoirs, as well as the current understanding of induced seismicity. An explanation of the method introduced in Petrini et al. (2020) is given in chapter 3, including adaptations to the code that were required for this study, a description of three base case model set-ups, and an overview of the parameters that were changed for the parameter study. The results are presented in chapter 4, which are discussed in chapter 5 and concluded in chapter 6.

Chapter 2

Background

2.1 Geothermal systems in the Netherlands

The 2021 annual review of 'natural resources and geothermal energy in the Netherlands' shows that at the time of publication 26 geothermal systems had been installed in the Netherlands of which 19 were active during 2021 (Ministry of Economic Affairs and Climate Policy (MEA) (2022)). The operational systems consist of geothermal doublets, triplets, and a quartet. These terms refer to the number of wells used in the geothermal system (i.e. a doublet refers to two wells, a triplet to three wells, and a quartet to four). This thesis will focus only on doublet systems as these are the most common in the Netherlands (Ministry of Economic Affairs and Climate Policy (MEA) (2022)).

2.1.1 Characteristics

Catalogs of geothermal systems have been created to distinguish between different types of geothermal plays (e.g. Moeck (2014) and Breede et al. (2015)). Mijnlieff (2020) uses these catalogs to characterize the typical Dutch geothermal play, which is summarized in this subsection.

As of yet, no reservoir stimulation (e.g. hydraulic fracturing) has been required to circulate geothermal fluids within the reservoir (i.e. a petrothermal system). The present systems rely on the natural porosity and permeability present within the reservoir (i.e. a hydrothermal system). The required permeability can come from the reservoir matrix, faults, or fractures. All current reservoirs can be described as permeable and porous sedimentary rocks in which heat is transported by means of conduction. These types of geothermal reservoirs are referred to as 'Hot Sedimentary Aquifers' (HSA).

A suitable HSA should meet certain requirements (Breede et al. (2015) and references therein): 1) The density of the aquifer cannot be higher than the crystalline basement and should be around 2400 kgm^{-3}. 2) A seal or cap rock is required as it acts as a thermal fluid insulator. 3) The permeability of a suitable hydrothermal system should be at least $10^{-14}m^2$.

The temperatures related to Dutch geothermal energy production are considered low. While the geothermal gradient (31 $^{\circ}CKm^{-1}$) can deviate slightly at certain locations, there are no hot spots or significant temperature anomalies recorded for the Dutch subsurface. The depths of the HSAs range from 500 to 3000 m, classifying these systems as 'deep geothermal' (between 400 and 4000 m) (figure 2.1). This results in production temperatures up to 100 $^{\circ}C$.

An ultra deep geothermal target that exists is the Dinantian Limestone. However, there is insufficient knowledge on the permeability, and the temperature- and

stress-gradients which makes this target a high risk (Boxem et al. (2016)). This thesis therefore only focuses on deep geothermal systems.

Strata that meet the requirements described above and could therefore potentially provide a suitable reservoir are: the Tertiary, the Chalk, Jurassic/Chalk, Triassic, the Rotliegend, and Upper Carboniferous plays (Stichting Platform Geothermie (2018)).

2.1.2 Geothermal energy production

A doublet comprises a production and an injection well (figure 2.1). At the surface these wells are linked to one another, forming a closed system for brine circulation. At subsurface levels, the ends of the wells are located in a single porous reservoir containing brine and have a suitable horizontal distance (1-2 km) between them to ensure that cool water is not pumped back up during the economic life time of a doublet (Stichting Platform Geothermie (2018)). The production well pumps up the reservoir water to the surface. Via a heat exchanger, the heat is transferred to a surface grid system, which transports the heat to consumers. The cooled, salt water is injected back into the reservoir. The injected water is then heated by the reservoir temperatures.

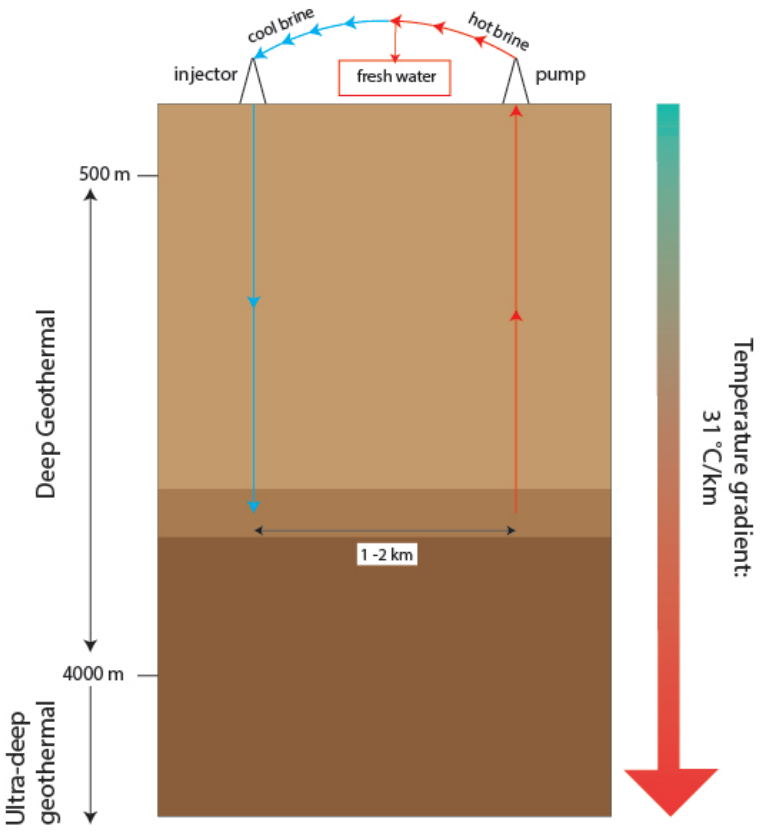

FIGURE 2.1: Schematic illustration of a doublet system.

2.2 Theory of induced seismicity

Induced seismicity is a term coined for any type of rock failure that is triggered by stress changes caused by human activities, such as: gas production, water or CO_2 injection, and geothermal operations. It is commonly thought that a pre-existing fault is required to induce seismicity and that stress changes due to these human activities re-activate these faults when the accumulated stresses surpass a failure criterion (e.g. Buijze et al. (2019) and Rathnaweera et al. (2020)). In this section, different factors will be introduced that have been considered to play a part in inducing seismicity.

2.2.1 Pore-fluid pressure changes

Increases and decreases in the pore-fluid pressure can affect the stress in a geothermal system directly as well as indirectly (e.g. Buijze et al. (2019)). When fluids are injected into a reservoir the pore-fluid pressure increases, this leads to a decrease in the effective pressure ($P^e = P^t - P^f$), meaning the rock matrix becomes weaker and closer to failure. As time progresses, the injected fluid percolates away from the well, raising fluid pressures farther away from the well and decreasing the effective pressure and strength farther away from the well. The ease with which the injected fluid can flow is determined by the matrix and fracture permeability.

Pore-fluid pressure changes can also affect the total stress through changes in volumetric strain, i.e. poro-elastic stressing (Biot (1941), Biot (1955), Biot (1956a), and Biot (1956b)). A rock volume expands as a result of the injected fluid, which builds up elastic strain and results in increased stress. The rock volume decreases at the production well, as fluid is being extracted here. The greatest volume increase is within the injection well, therefore the largest poro-elastic stresses are found here. Furthermore, the accumulated stresses can result in the (plastic) collapse of the pore space (Yarushina et al. (2015)).

2.2.2 Temperature changes

The method in this thesis ignores the effects of temperature, nevertheless, it is important to understand how temperature affects the stress in geothermal systems. As fluid is injected the temperature around the well drops, which leads to thermal contraction which decreases the stress (Buijze et al. (2019)). This results in increased stresses in the rock masses adjacent to the well.

The effect of the temperature is not yet investigated as this thesis is focused on the coupling between solid deformation and fluid flow. Incorporating the temperature effect will complicate the results as it will be more difficult to discern what is influencing the stress more: fluid pressure or fluid temperature.

2.2.3 Chemical changes

Chemical alterations can occur within a reservoir when fluid is injected. These alterations can result in a decrease in the cohesion and friction coefficient of rocks (Rathnaweera et al. (2020)). This reduces the strength of the rock, bringing it closer to failure. The effect of chemical changes is not examined in this thesis. As mentioned above, the focus lies on the solid-fluid coupling.

Chapter 3

Methods

The code used for this thesis was first introduced in Petrini (2019) and Petrini et al. (2020). It is a 2D, finite difference, seismo-hydro-mechanical numerical code, in which fluid flow is coupled to solid deformation. This is based on Biot's poro-elastic theory, which couples solid and fluid deformation with linear and reversible elastic relations (Biot (1941), Biot (1955), Biot (1956a), and Biot (1956b)). This theory was expanded by Yarushina et al. (2015), in which conservation equations are introduced that take irreversible responses, such as pore collapse, into consideration. The code was first used to investigate the effect of solid-fluid coupling in a subduction zone and later adapted to investigate a simple setting in which fluid injection is simulated (figure 3.1), henceforth referred to as 'the Petrini code' (Petrini (2019)).

Preliminary tests are used to debug the Petrini code, after which three base case models are set up in this thesis: 1) a model with a single injection well, 2) a model with a doublet, and 3) a model with a doublet with a fault. The third base case is used as a reference model for a small parameter study in which the effects of production parameters and fault material properties are examined.

Sections 3.1 to 3.5 summarize the method introduced in Petrini (2019) after which the adaptations that were made to the Petrini code are described.

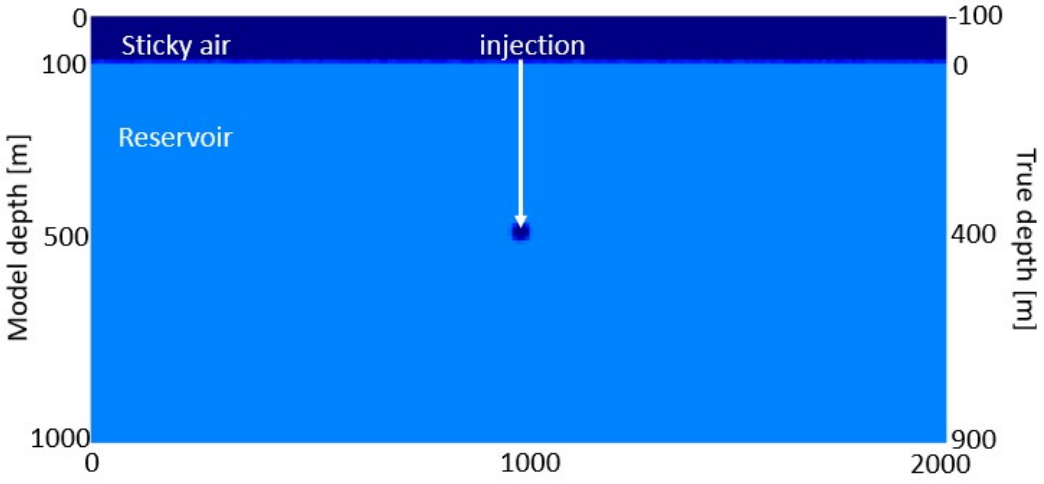

FIGURE 3.1: The Petrini code set-up, including a single layer reservoir with an injection well at the center of the model. The model depth starts below the upper boundary of the model, while the 'true' depth would start below the sticky air layer, which is used to simulate the free surface. The model used a resolution of 10 m in both the x and y direction.

3.1 Governing Equations

The code solves for the conservation of total momentum (i.e. solid matrix + fluid, equation 3.1), solid mass (equation 3.2, fluid momentum (equation 3.3), fluid mass (equation 3.4), with variable porosity based on equation 3.5 (Petrini (2019),Yarushina et al. (2015), and Gerya (2019)). The definitions of the symbols in these equations can be found in the 'List of Symbols'.

$$\frac{\partial \sigma'^{t}_{ij}}{\partial x_j} - \frac{\partial P^t}{\partial x_j} + \rho^t g_i = (1-\varphi)\rho^s \frac{D^s v^s_i}{Dt} + \varphi \rho^f \frac{D^f v^f_i}{Dt} \tag{3.1}$$

$$\nabla \cdot v^s = -\frac{1}{K^d}\left(\frac{D^s P^t}{Dt} - \alpha \frac{D^f P^f}{Dt}\right) - \frac{P^t - P^f}{\eta^\varphi (1-\varphi)} \tag{3.2}$$

$$v^D_i = -\frac{k^\varphi}{\eta^f}\left(\nabla P^f - \rho^f g_i + \rho^f \frac{D^f v^f_i}{Dt}\right) \tag{3.3}$$

$$\nabla \cdot v^D = \frac{\alpha}{K^d}\left(\frac{D^s P^t}{Dt} - \frac{1}{\beta}\frac{D^f P^f}{Dt}\right) + \frac{P^t - P^f}{\eta^\varphi (1-\varphi)} \tag{3.4}$$

$$\frac{D^s ln\frac{(1-\varphi)}{\varphi}}{Dt} = \frac{1}{K^\varphi (1-\varphi)\varphi}\left(\frac{D^s P^t}{Dt} - \frac{D^f P^f}{Dt}\right) + \frac{P^t - P^f}{\eta^\varphi (1-\varphi)\varphi} \tag{3.5}$$

The difference in solid and fluid acceleration is assumed to be negligible (i.e $\frac{D^f v^f_i}{Dt} \approx \frac{D^s v^s_i}{Dt}$), the difference was proven to be very small in numerical experiments (Petrini (2019)). Applying this assumption to equation 3.1, yields:

$$\frac{\partial \sigma'_{ij}}{\partial x_j} - \frac{\partial P^t}{\partial x_j} + \rho^t g_i = \rho^t \frac{D^s v^s_i}{Dt} \tag{3.6}$$

The connected porosity (φ, isolated pores are considered to be part of the solid matrix as they have no influence on fluid flow) influences the conservation equations directly. However, many of the material properties in these equations are also dependent on the porosity, either linearly or non-linearly.

Darcy's velocity (v^D), or *Darcy flux*, describes the flux of a volume of fluid relative to the moving solid phase (Gerya (2019)), and can also be expressed as:

$$v^D_i = \varphi(v^f_i - v^s_i) \tag{3.7}$$

The subscript i implies the i-th component of the velocity vectors and the superscripts f and s stand for fluid and solid respectively. The total pressure (P^t), total density (ρ^t), and total deviatoric stress (σ'^t_{ij}) can be expressed as the sum of the fluid and solid properties multiplied with their fraction of the total material:

$$P^t = P^f \varphi + P^s (1-\varphi) \tag{3.8}$$

$$\rho^t = \rho^f \varphi + \rho^s (1-\varphi) \tag{3.9}$$

$$\sigma'^t_{ij} = \sigma'^f_{ij} \varepsilon + \sigma'^s_{ij} (1-\varphi) \tag{3.10}$$

k^{φ} is the permeability, which has a non-linear relationship with the porosity:

$$k^{\varphi} = k_r^{\varphi} \left(\frac{\varphi}{\varphi_r} \right)^m \left(\frac{1-\varphi}{1-\varphi_r} \right)^n \tag{3.11}$$

k_r^{φ} is the permeability at a reference porosity (φ_r), the exponents m and n take the value of 3 and 0 (respectively), eliminating the second term.

The effective viscosity (η^{φ}) depends on the effective shear viscosity of the solid matrix (η^s), the pore geometry, and the porosity:

$$\eta^{\varphi} = \frac{2m}{(m+1)} \frac{\eta}{\varphi} \tag{3.12}$$

here, m is a geometrical factor that can be either 1 or 2 for cylindrical and spherical pores, respectively (Yarushina et al. (2015)). In this research, m takes the value of 1, reducing equation 3.12 to:

$$\eta^{\varphi} = \frac{\eta}{\varphi} \tag{3.13}$$

Furthermore, the effective shear viscosity (η) is exponentially dependent on the porosity:

$$\eta = \eta^s e^{-\alpha_v \varphi} \tag{3.14}$$

where η^s is the shear viscosity of solid grains and α_v is an experimentally derived porosity weakening factor, which is 29 in this study (Petrini (2019) and Petrini et al. (2020))

The Biot-Willis coefficient (α) is defined as follows (Yarushina et al. (2015)):

$$\alpha = 1 - \frac{K^d}{K^s} \tag{3.15}$$

The equations for the drained and effective bulk moduli are calculated respectively:

$$K^d = (1-\varphi) \left(\frac{1}{K^{\varphi}} + \frac{1}{K^s} \right)^{-1} \tag{3.16}$$

$$K^{\varphi} = \frac{2m}{(m+1)} \frac{\mu}{\varphi} = \frac{\mu}{\varphi} \text{ as m = 1} \tag{3.17}$$

The shear modulus (μ) is, furthermore, dependent on the porosity, according to:

$$\mu = \mu^0 (1-\varphi) \tag{3.18}$$

μ^0 is the shear modulus of the solid rock grains.

The Skempton's coefficient (β) is defined as:

$$\beta = \frac{\frac{1}{K^d} - \frac{1}{K^s}}{\frac{1}{K^d} - \frac{1}{K^s} + \varphi \left(\frac{1}{K^f} - \frac{1}{K^s} \right)} \tag{3.19}$$

The porosity is updated after every time step, based on equation 3.5:

$$\Delta\varphi = \frac{D^s ln \left(\frac{1-\varphi}{\varphi} \right)}{Dt} \tag{3.20}$$

with the subscript m referring to a single marker. The new porosity can then be computed:

$$\varphi^{new} = \frac{\varphi(1-\varphi)}{e^{(\Delta\varphi dt)} + \varphi} \tag{3.21}$$

An updated porosity will affect all material parameters that are influenced by the porosity, mentioned above.

The importance of the porosity and permeability was highlighted in Petrini et al. (2020), as well as the preliminary tests (appendix A).

3.2 Rheological Model

A visco-elasto-plastic Maxwell rheology is used for the solid matrix (Gerya (2019), Petrini (2019), and Petrini et al. (2020)). The deviatoric strain rate is defined as the strain rate tensor (equation 3.22) minus the sum of the diagonal ($\dot{\varepsilon}_{kk}$), which is the rate of volume change (equation 3.23).

$$\dot{\varepsilon}_{ij} = \frac{1}{2}\left(\frac{\partial v_i^s}{\partial x_j} + \frac{\partial v_j^s}{\partial x_j}\right) \tag{3.22}$$

$$\dot{\varepsilon}'_{ij} = \dot{\varepsilon}_{ij} - \dot{\varepsilon}_{kk} = \frac{1}{2}\left(\frac{\partial v_i^s}{\partial x_j} + \frac{\partial v_j^s}{\partial x_j}\right) - \frac{1}{3}\delta_{ij}\nabla \cdot v^s \tag{3.23}$$

The bulk deviatoric strain rate (equation 3.23) is further defined as the sum of the three respective components :

$$\dot{\varepsilon}'_{ij} = \dot{\varepsilon}'_{ij(viscous)} + \dot{\varepsilon}'_{ij(elastic)} + \dot{\varepsilon}'_{ij(plastic)} \tag{3.24}$$

where

$$\dot{\varepsilon}^{'}_{ij(viscous)} = \frac{1}{2\eta}\sigma^{'}_{ij} \tag{3.25}$$

$$\dot{\varepsilon}^{'}_{ij(elastic)} = \frac{1}{2\mu}\frac{D\sigma^{'}_{ij}}{Dt} \tag{3.26}$$

$$\begin{aligned}\dot{\varepsilon}^{'}_{ij(plastic)} &= 0 \text{ for } \sigma_{II} < \sigma_{yield} \\ &= \chi\frac{\delta G_{plastic}}{\delta\sigma^{'}_{ij}} = \chi\frac{\sigma^{'}_{ij}}{2\sigma^{'}_{II}} \text{ for } \sigma_{II} = \sigma_{yield}\end{aligned} \tag{3.27}$$

The definitions of the symbols used in these equations can be found in the List of Symbols.

The plastic flow potential ($G_{plastic}$), which describes the amount of mechanical energy per unit volume that supports plastic deformation, can be defined as:

$$G_{plastic} = \sigma_{II} \tag{3.28}$$

$$\sigma_{II} = \sqrt{\frac{1}{2}\sigma'^{2}_{ij}} \tag{3.29}$$

where σ_{II} is the second invariant of the stress tensor, which is limited by the yielding stress (σ_{yield}), according to the Drucker-Prager yielding condition (Drucker and

Prager (1952), Gerya (2019), Petrini (2019), and Petrini et al. (2020)):

$$\sigma_{II,max} = \sigma_{yield} \tag{3.30}$$

$$\begin{aligned} \sigma_{yield} &= \sigma_c + \gamma_{int}(P^t - P^f) \text{ when } P^t - P^f > \frac{\sigma_c - \sigma_t}{1 - \gamma_{int}} \\ &= \sigma_t + (P^t - P^f) \text{ when } P^t - P^f < \frac{\sigma_c - \sigma_t}{1 - \gamma_{int}} \end{aligned} \tag{3.31}$$

γ_{int} is the internal friction coefficient, which is equal to $sin(\phi)$ (ϕ is the angle of internal friction), σ_c is the compressive strength and σ_t is the tensile strength (Gerya (2019)). The first condition in equation 3.31 is the yielding of confined (compressive) fractures, while the second condition describes the yielding of tensile fractures. The compressive and tensile strength are related to the porosity:

$$\sigma_c = \sigma_{c,0}\,(1 - \varphi) \tag{3.32}$$

$$\sigma_t = \sigma_{t,0}\,(1 - \varphi) \tag{3.33}$$

The plastic multiplier is a coefficient that is obtained locally at each time step by solving equations 3.24-3.30. Petrini (2019) derives that the plastic multiplier is equal to:

$$\chi = 2\dot{\varepsilon}^{'}_{II(plastic)} \tag{3.34}$$

where $\dot{\varepsilon}^{'}_{II(plastic)}$ is the second invariant of the deviatoric strain rate tensor:

$$\dot{\varepsilon}^{'}_{II(plastic)} = \sqrt{\frac{1}{2}\dot{\varepsilon}^{'}_{ij(plastic)}} \tag{3.35}$$

A reformulation of equation 3.24 is beneficial for easy implementation into the code:

$$\dot{\varepsilon}^{'}_{ij} = \dot{\varepsilon}^{'}_{ij(viscous)} + \dot{\varepsilon}^{'}_{ij(elastic)} + \dot{\varepsilon}^{'}_{ij(plastic)} = \frac{1}{2\eta_{vp}}\sigma^{'}_{ij} + \dot{\varepsilon}^{'}_{ij(elastic)} \tag{3.36}$$

Where the visco-plastic viscosity (η_{vp}) combines plastic and viscous deformation:

$$\eta_{vp} = \begin{cases} \eta & \text{for } \sigma^{'}_{II} < \sigma_{yield} \\ \eta\frac{\sigma^{'}_{II}}{\sigma^{'}_{II} + \chi\eta} = \eta\frac{\sigma^{'}_{II}}{\sigma^{'}_{II} + 2\dot{\varepsilon}_{II(plastic)}\eta} & \text{for } \sigma^{'}_{II} = \sigma_{yield} \end{cases} \tag{3.37}$$

A visco-elasto-plastic stress relation is derived from equation 3.36 (Petrini (2019)):

$$\sigma^{\prime}_{ij} = 2\eta_{vp}\dot{\varepsilon}^{\prime}_{ij}Z + \sigma^{\prime\,0}_{ij}(1 - Z) \tag{3.38}$$

where σ^{0}_{ij} is the deviatoric stress of the previous time step (corrected for advection and rotation), Δt is the computational time step, and Z is the visco-elasticity factor:

$$Z = \frac{\mu\Delta t}{\mu\Delta t + \eta_{vp}} \tag{3.39}$$

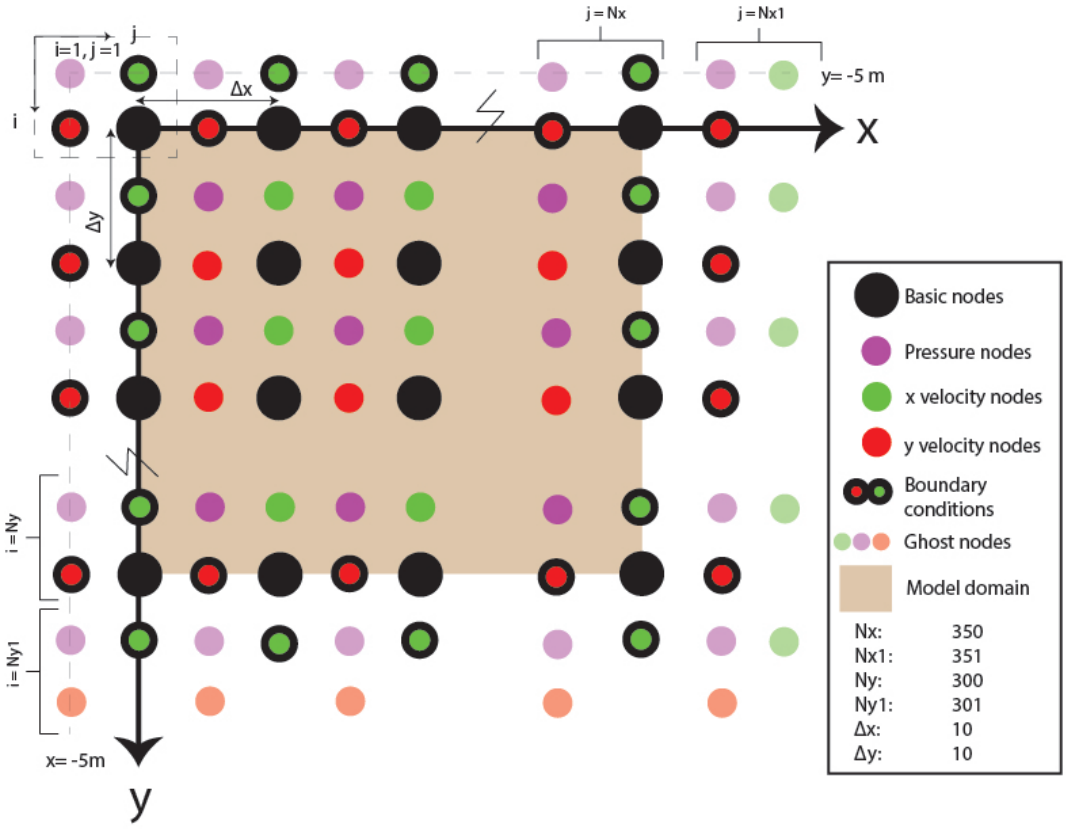

FIGURE 3.2: 2D staggered grid, with the different types of nodes, indexed with i in the y-direction and j in the x-direction. All nodes have a spacing of 10 m (Δx and Δy). Ghost nodes (faded) are set to zero and are not used in any numerical solutions, they offer uniformity in the numbering (Gerya (2019)). 'Free slip' boundary conditions are set on all the boundaries: the velocity component that is perpendicular to the boundary is zero and the other component does not change along the boundary.

3.3 Model structure

The code uses a 2D fully staggered Eulerian grid for the discretization of the conservation equations (figure 3.2). Figure 3.2 conveys the different nodes on which the different variables are stored: basic nodes (black), pressure nodes (purple), x-velocity nodes (green), and y-velocity nodes (red). This allows for an optimal and accurate discretization of the 2D momentum and mass conservation equations. Furthermore, the code makes use of randomly distributed Lagrangian markers for the transportation of material properties (figure 3.3). The initial conditions are stored on the markers, after which the information they carry is interpolated to the nodes, based on the weighted average:

$$B_{(i,j)} = \frac{\sum_m B^m w^m_{(i,j)}}{\sum_m w^m_{(i,j)}} \tag{3.40}$$

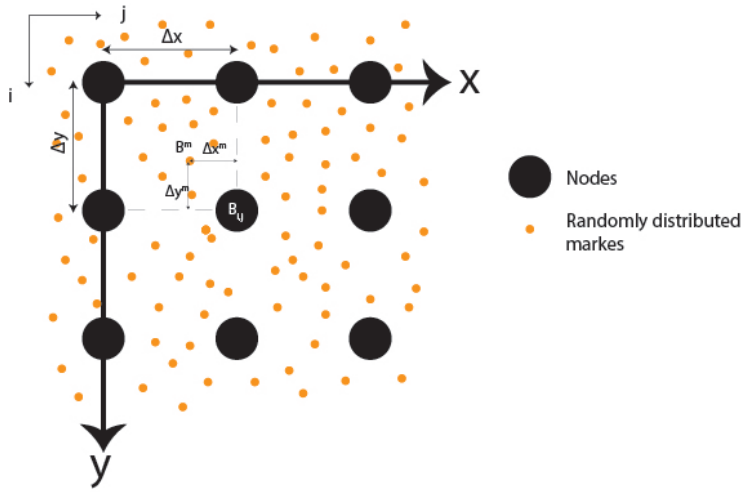

FIGURE 3.3: The stencil that is used to interpolate properties from marker B^m to node B_{ij}, which is located at a distance of Δx^m and Δy^m in the x- and y-directions respectively.

the weighted average (w^m) is dependent on the distance between the marker and node:

$$w^m_{(i,j)} = \left(1 - \frac{\Delta x^m}{\Delta x}\right)\left(1 - \frac{\Delta y^m}{\Delta y}\right) \tag{3.41}$$

here $B_{(i,j)}$ and B^m respectively represent the nodal and marker values of a random parameter B and Δx^m and Δy^m are the distance from marker to node in the x- and y-direction respectively (figure 3.3).

After each time step, updated information is passed back from the nodes to the markers:

$$B^m = w^m_{(i,j)}B_{(i,j)} + w^m_{(i-1,j)}B_{(i-1,j)} + w^m_{(i,j-1)}B_{(i,j-1)} + w^m_{(i-1,j-1)}B_{(i-1,j-1)} \tag{3.42}$$

Subsequently, each marker is transported to a new position according to the velocity field that was computed within the time step. Now, a new quantity (B^a) is re-interpolated from the markers to the nodes. ΔB is calculated:

$$\Delta B = B^a - B^n \tag{3.43}$$

where B^n is the nodal quantity before the markers moved. Finally, the nodal quantity B is updated:

$$B = B + \Delta B \tag{3.44}$$

3.4 Injection

Fluid injection is only imposed on a pressure node at the center of the injection well (figure 3.1), implemented into equation 3.4 (Petrini (2019)):

$$\nabla \cdot v^D + \nabla \cdot v^{inject} = \frac{\alpha}{K^d}\left(\frac{D^s p^t}{Dt} - \frac{1}{\beta}\frac{D^f p^f}{Dt}\right) + \frac{p^t - p^f}{\eta^\varphi(1-\varphi)} \tag{3.45}$$

where $\nabla \cdot v^{inject}$ is an initial value of the divergence of the injection fluid that is adapted based on the following set of equations (figure 3.5):

$$P_{well}^{req} = P_{well}^{initial} + \dot{P}^{injection} * t_{sum} \tag{3.46}$$

$$\Delta P_{well} = \frac{P_{well}^{req} - P_{well}^{cur}}{\dot{P}^{injection} * tsum} \tag{3.47}$$

$$\nabla \cdot v_{new}^{inject} = \nabla \cdot v_{old}^{inject} * (1 + \Delta P_{well}) \tag{3.48}$$

P_{well}^{req} is the expected well pressure based on a defined pressure injection rate ($\dot{P}^{injection}$) and the total amount of time that injection has been imposed (t_{sum}). The divergence of the injection fluid velocity is updated based on the deviation (ΔP_{well}) between the expected well pressure and the actual well pressure (P_{well}^{cur}). For the production well a negative initial $\nabla \cdot v^{injection}$ is chosen and as well as a negative pressure rate.

3.5 Adaptive time-stepping and global Picard iterations

In order to solve the nonlinear equations accurately, adaptive time-stepping and global Picard iterations are introduced. After each time step the displacement, velocity, and porosity changes are evaluated. If these values are above a predefined cutoff value and/or the yielding condition is met (equations 3.30), iterations will commence with increasingly smaller time step sizes until all conditions are stable. The code will then continue as normal with the smaller time step size.

a)

```
% Compute stress and strain rate invariants and dissipation
% Process pressure cells
for i=2:1:Ny
  for j=2:1:Nx
    % EXY term is averaged from four surrounding basic nodes
    EXY2=(EXY(i,j)^2+EXY(i-1,j)^2+EXY(i,j-1)^2+EXY(i-1,j-1)^2)/4;
    EII(i,j)=(EXX(i,j)^2+EXY2)^0.5;
    EXYVP2=((SXY(i,j)/2/ETA(i,j))^2+(SXY(i-1,j)/2/ETA(i-1,j))^2+(SXY(i,j-1)/2/ETA(i,j-1))^2+(SXY(i-1,j-1)/2/ETA(i-1,j-1))^2)/4;
    EIIVP(i,j)=((SXX(i,j)/2/ETAP(i,j))^2+EXYVP2)^0.5;
    % Second strain rate invariant SII
    % SXY term is averaged from four surrounding basic nodes
    SXY2=(SXY(i,j)^2+SXY(i-1,j)^2+SXY(i,j-1)^2+SXY(i-1,j-1)^2)/4;
    SII(i,j)=(SXX(i,j)^2+SXY2)^0.5;
```

b)

```
% Compute stress and strain rate invariants and dissipation
% Process pressure cells
for i=2:1:Ny
  for j=2:1:Nx
    % EXY term is averaged from four surrounding basic nodes
    EXY2=(EXY(i,j)+EXY(i-1,j)+EXY(i,j-1)+EXY(i-1,j-1))/4;
    EII(i,j)=(EXX(i,j)^2+EXY2^2)^0.5;
    EXYVP2=((SXY(i,j)/2/ETA(i,j))+(SXY(i-1,j)/2/ETA(i-1,j))+(SXY(i,j-1)/2/ETA(i,j-1))+(SXY(i-1,j-1)/2/ETA(i-1,j-1)))/4;
    EIIVP(i,j)=((SXX(i,j)/2/ETAP(i,j))^2+EXYVP2^2)^0.5;
    % Second strain rate invariant SII
    % SXY term is averaged from four surrounding basic nodes
    SXY2=(SXY(i,j)+SXY(i-1,j)+SXY(i,j-1)+SXY(i-1,j-1))/4;
    SII(i,j)=(SXX(i,j)^2+SXY2^2)^0.5;
```

FIGURE 3.4: The calculation of the second invariant of the deviatoric stress tensor (SII), the second invariant of the deviatoric strain rate (EII), and the second invariant of the deviatoric visco-plastic strain rate (EIIVP) in the a) original code and b) the adapted code.

3.6 Adaptations to the Petrini code

Some changes are imposed on the Petrini code. One change that has been made to the Petrini code has to do with the way average values are calculated in order to derive a value from one type of node to another (e.g. from the basic nodes to the pressure nodes). An example of this is shown in figure 3.4.a, the Petrini code uses a root mean square calculation to find average values from the surrounding basic nodes to interpolate them to the pressure node. The arithmetic mean is a more logical option to calculate the average values, therefore this has been changed in the code that has been used for this thesis (figure 3.4.b).

Another change is implemented in the adaptation of the $\nabla \cdot v^{injection}$ (figure 3.5). In the original code, the initial well pressure was incorrectly defined, as the node indices (i and j) are only specified for the condition that the time-sum is larger than the injection start time. The indices that were used originally took the value of the last values for i and j which were the indices of the node at the right bottom of the model. This resulted in instabilities in the velocities in preliminary tests (figure 3.6.a), which led to instabilities in other parameters, such as the strain rate. The adaptation (figure 3.5.b) ensures that the initial well pressure is defined correctly. Once implemented, the instabilities that arose in the preliminary tests were resolved (figure 3.6.b).

One goal of this thesis is to identify and resolve mistakes or inefficiencies in the code. Mistakes that have not been removed before running the base case models and the parameter study will therefore be reported and discussed in chapters 4 and 5 respectively.

a)

```
% Change injection conditions
if(timesum>tinject)
    j=fix((xwell-xp(1))/dx)+1;
    i=fix((ywell-yp(1))/dy)+1;
    % Compute current and required pressure, Pa
    prequired=pinitial+dpdtinject*(timesum+dt-tinject)
    pcurrent=pf(i,j)
    % Check relative pressure difference
    deltadp=(prequired-pcurrent)/(timesum+dt-tinject)/dpdtinject
    divinject=divinject*(1+min(dpmax,max(-dpmax,deltadp)))
%         pause(5)
else
    % Set initial pressure
    pinitial=pf(i,j);
end
```

b)

```
% Change injection conditions
if(timesum>tinject)
    j=fix((xwell1-xp(1))/dx)+1;
    i=fix((ywell1-yp(1))/dy)+1;

    % Compute current and required pressure, Pa
    prequired=pinitial+dpdtinject*(timesum+dt-tinject)
    pcurrent=pf(i,j)
    % Check relative pressure difference
    deltadp=(prequired-pcurrent)/(timesum+dt-tinject)/dpdtinject
    divinject=divinject*(1+min(dpmax,max(-dpmax,deltadp)))
else
    % Set initial pressure
    j=fix((xwell1-xp(1))/dx)+1;
    i=fix((ywell1-yp(1))/dy)+1;

    pinitial=pf(i,j);
end
```

FIGURE 3.5: The adaptation on the $\nabla \cdot v^{inject}$ (divinject) based on the difference between the required (prequired) and the current (pcurrent) well pressure in the a) original code and b) the adapted code.

a)

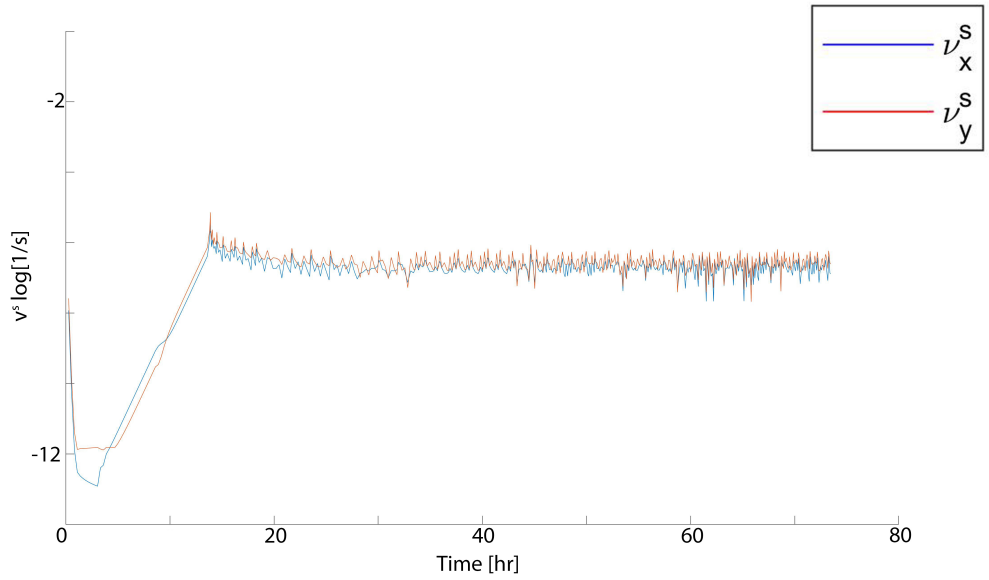

b)

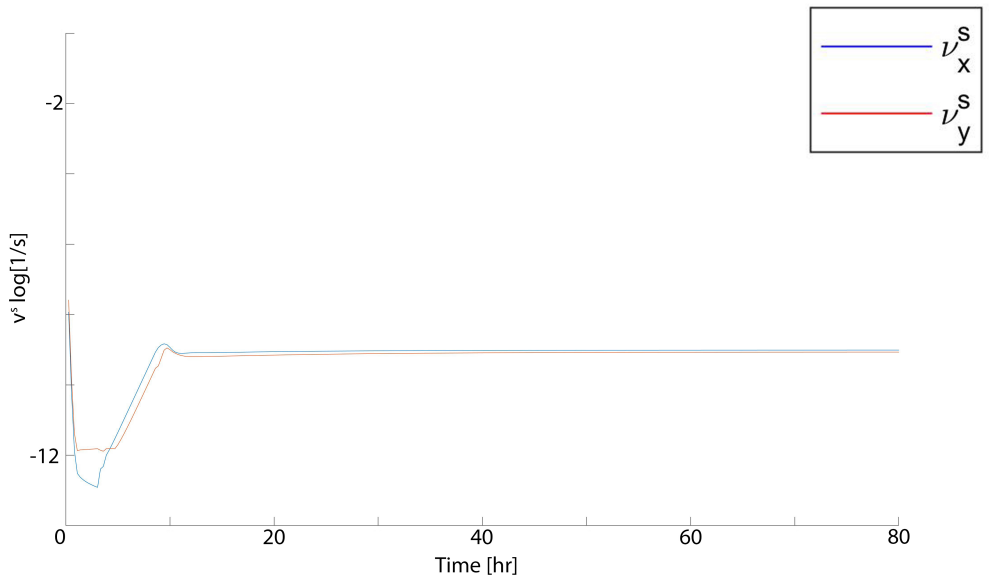

FIGURE 3.6: a) an instability in the velocity caused by an improper definition of the initial well pressure, b) the instability is resolved once the initial well pressure is defined correctly.

3.7 Model Set-up

Three base cases are examined: 1) a model with a single injection well, 2) a model with an injection and extraction well (doublet system), and 3) a model with an injection and extraction well with a fault crossing all layers in between. The material parameters used in the base cases are listed in table 3.1. Note that the parameters in table 3.1 are the initial values for these parameters before the porosity influences (e.g. equation 3.32) have been implemented. A similar set-up with similar material parameters was used as in van Wees et al. (2020) (figures 3.7 and 3.8). This set-up leads to an initial total pressure gradient of 0.022 MPa/m (2.2 Bar/10m) and a fluid

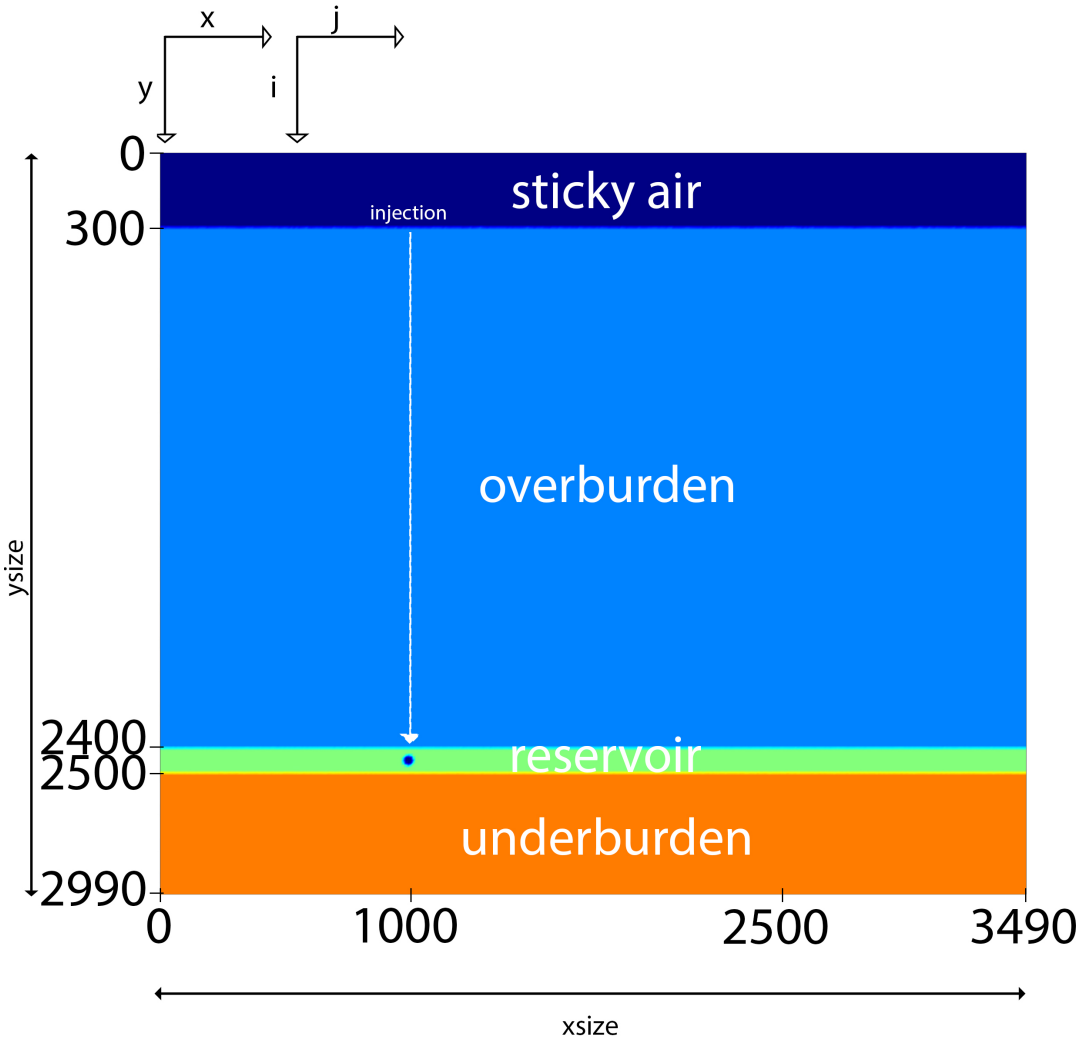

FIGURE 3.7: Base case 1: a model with only an injection well, the set-up is based on the model used in van Wees et al. (2020).

pressure gradient of 0.01 MPa/m (1 Bar/10m). These gradients are common for the south of the Netherlands (e.g. Van Wees et al. (2014)).

All models are 3490 m wide (xsize) and have a maximum depth of 2990 m (ysize), with a resolution of 10x10 m. The injection well is always located at 1000 m from the left boundary and the production well is located at 1500 m horizontal distance from the injection well. The reservoir starts at 2400 m and has a thickness of 100 m. Both wells are placed at an equal distance to the boundary, for the reference models both wells are located at 2450 m below the upper boundary.

Base case 1 uses a pressure rate of +1 Pa/s and an initial divergence of injection velocity or 1e-10 s^{-1}. The same initial divergence is used in all models, as this value is corrected within the code, based on the pressure rate (equations 3.46 - 3.48). The pressure rate is an estimation based on a typical injection and production rate of 300 m3/h ($\approx 0.08 m^3/s$) (van Wees et al. (2020)). The injection well has a radius of 20m, if the well were 3D the area that would be influenced by injection would be:

$$A_{well} = \pi R^2 = \pi 20^2 \approx 1300 m^2 \tag{3.49}$$

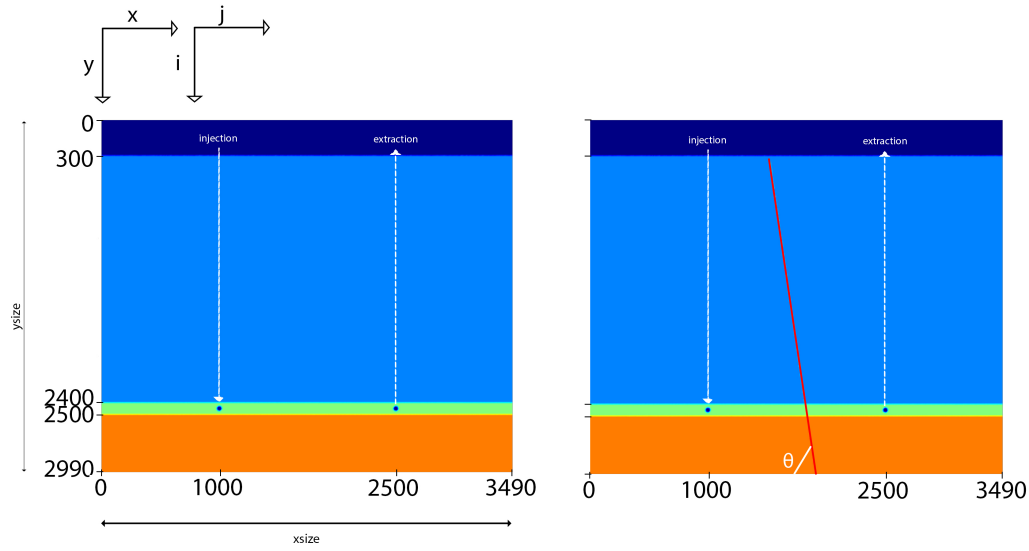

FIGURE 3.8: Base case 2 (left): a model with an injection and a production well. Base case 3 (right): a model with an injection and a production well with a fault (red), with a dip (θ) of 70 °. The set-up is based on the model used in van Wees et al. (2020).

The mass that's injected per second is:

$$m_{inject} = \rho_f * V_{inject} = 1000 \cdot 0.08 = 80kg \tag{3.50}$$

The estimated pressure that is injected per second, follows:

$$P_{inject} = \frac{m_{inject} g}{A_{well}} \approx 1Pa \tag{3.51}$$

Base cases 2 and 3 use a pressure rate of +1 Pa/s at the injection well and -1 Pa/s at the production well. The initial divergence of injection velocity at the production well is -1e-10 1/s.

3.7.1 Boundary Conditions

All scenarios implement a 'free slip' condition on all boundaries (figure 3.2) and make use of the "sticky air" approach. This approach is used to simulate the free surface by using a low viscosity ($1 \cdot 10^{-3}$ [Pa·s]) and low rock density (1000 [$\frac{Kg}{m^3}$]), and the thickness is equal to 10% of the size of the y-domain, which is 299 m for all models (figure 3.7). The sticky air will always behave purely viscously due to the very low viscosity of this layer, which will ensure that no elastic stresses will build at the surface. All other sticky air material parameters can be found in table 3.1. Note that because of this sticky air layer there is a distinction between 'model depth' and 'true depth', with 'model depth' referring to the depth below the upper boundary, where as 'true depth' refers to the depth below the free surface (figure 3.1), henceforth all references to depth will use the 'model depth' frame of reference.

3.7.2 Defining the fault

Base case 3 is the reference model for the parameter study. The fault in this model is defined as a zone with half the compressive and tensile strength of the surrounding

TABLE 3.1: Material parameters for all models, based on the parameters used in van Wees et al. (2020)

Parameters	Sticky Air	Over-/under-burden	Reservoir	Units
Solid density (ρ^s)	1000	2450	2450	$\frac{kg}{m^3}$
Shear viscosity of solid rock grains (η^0)	1e-3	1e21	1e21	$Pa \cdot s$
Porosity (φ)	5	5	15	%
Reference Porosity (φ_r)	1	1	1	%
Reference Permeability (k_r^{φ})	3e-16	1e-16	3e-13	m^2
Shear modulus of the solid rock grains (μ^0)	7.6e9	7.6e9	7.6e9	Pa
Compressive strength ($\sigma_{c,0}$)	7e6	7e6	7e6	Pa
Tensile strength ($\sigma_{t,0}$)	4.2e6	4.2e6	4.2e6	Pa
Internal friction coefficient (γ_{int})	0.5	0.5	0.5	-
Fluid density (ρ^f)	1000	1000	1000	$\frac{kg}{m^3}$
Fluid bulk modulus	2.5e9	2.5e9	2.5e9	Pa
Fluid viscosity	2e-4	2e-4	2e-4	$Pa \cdot s$

rocks. This is imposed on markers that exist within the imposed fault-zone. This is done, rather than considering the fault as a homogeneous material. The fault starts at 50 m beneath the boundary with the air, has a dip (θ) of 70°, a width of 1 m, and crosses all layers. The throw (vertical fault displacement) in base case 3 is 0 m (figure 3.8).

When the fault markers are interpolated to the nodes according to equations 3.40 and 3.41 the nodes that make up the fault will include both the weaker and original compressive and tensile strengths, as the width of the fault is smaller than the resolution. The compressive strength is not 0 for this base case, considering that most faults in the Netherlands have been inactive for a considerable amount of time and healing may have occurred (Buijze et al. (2017)). However, this is a parameter that will be examined in more detail in this study. The resulting strengths are rather variable along the fault due to this definition of the fault (3.9).

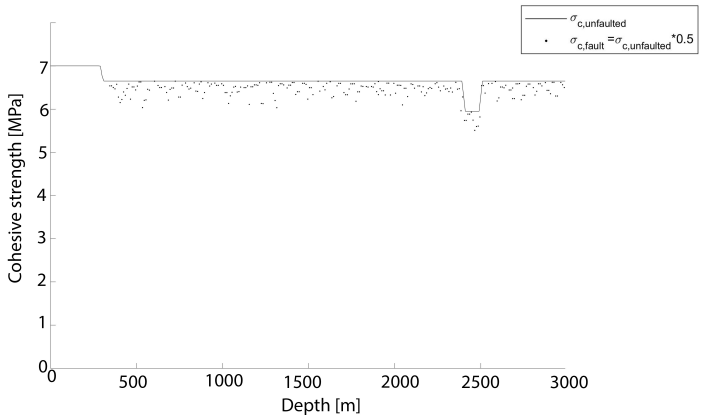

FIGURE 3.9: Cohesive strength of the surrounding rock (straight line) and cohesive strength on the fault markers (note that the cohesive strength that is plotted here already has been corrected for porosity according to equation 3.32).

All other material parameters for the fault markers in base case 3 are the same as the surrounding rocks, as is listed in table 3.1.

3.8 Parameter Study

Base case 3 was used as a reference model for the parameter study. All changes in parameters are therefore changes with respect to this base case. The parameters that are studied are: pressure rate (table 3.2), fault throw (table 3.3), fault permeability (table 3.4), fault porosity (table 3.5), and fault strength (table 3.6). The set-up for most of these models looks like figure 3.8, however, the set-up for the fault throw tests can be found in figure 3.10.

TABLE 3.2: Tested pressure rates

model	pressure rate
reference	$\pm 1 Pa/s$
1	$\pm 0.01 Pa/s$
2	$\pm 0.1 Pa/s$
3	$\pm 10 Pa/s$
4	$\pm 100 Pa/s$

TABLE 3.3: Tested fault throws

model	fault throw
reference	$0m$
1	$25m$
2	$50m$
3	$90m$
4	$110m$

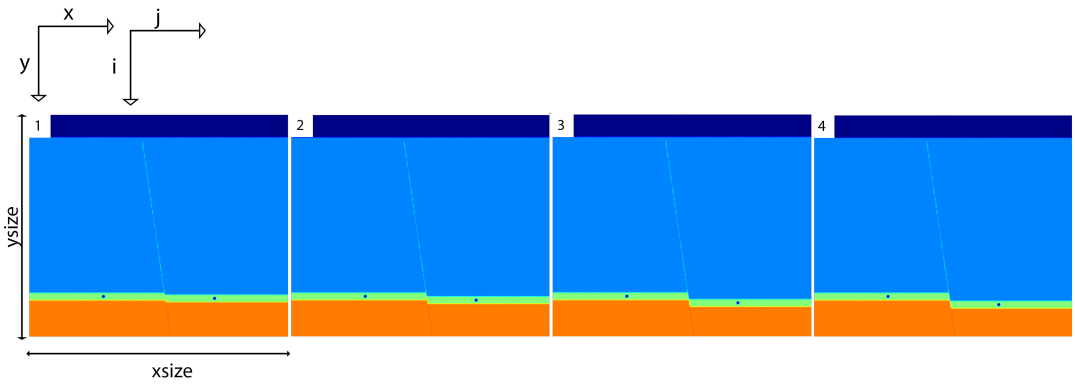

FIGURE 3.10: Model set-ups with varying throws, the numbers correspond to the model numbers in table 3.3

TABLE 3.4: Tested fault permeabilities

model	fault marker permeability
reference	equal to surrounding rock
1	10 x smaller than surrounding rock
2	5 x smaller than surrounding rock
3	5 x larger than surrounding rock
4	10 x larger than surrounding rock

TABLE 3.5: Tested fault porosities

model	fault marker porosity
reference	equal to surrounding rock
1	10% smaller than surrounding rock
2	5% smaller than surrounding rock
3	5% larger than surrounding rock
4	10% larger than surrounding rock

TABLE 3.6: Tested fault strengths

model	fault marker compressive/tensile strength
reference	0.5 x surrounding rock
1	0 x surrounding rock
2	0.20 x surrounding rock
3	0.60 x surrounding rock
4	0.90 x surrounding rock

Chapter 4

Results

4.1 Base case 1: single well model

4.1.1 Fluid velocity field

Fluid injection results in an asymmetric, divergent velocity field: with fluid flowing more rapidly to the right of the well (figure 4.1). Some extra experiments were run to discover the cause of this asymmetry.

A divergent velocity field, that is symmetric for both the y and x components, was found for a model that had the injection well in the center of the reservoir (figure 4.1). Furthermore, symmetry for the x-components was found for models that did not have an overburden or under-burden (figure 4.1), although a stronger upward flow is found for these models. This is further discussed in chapter 5.

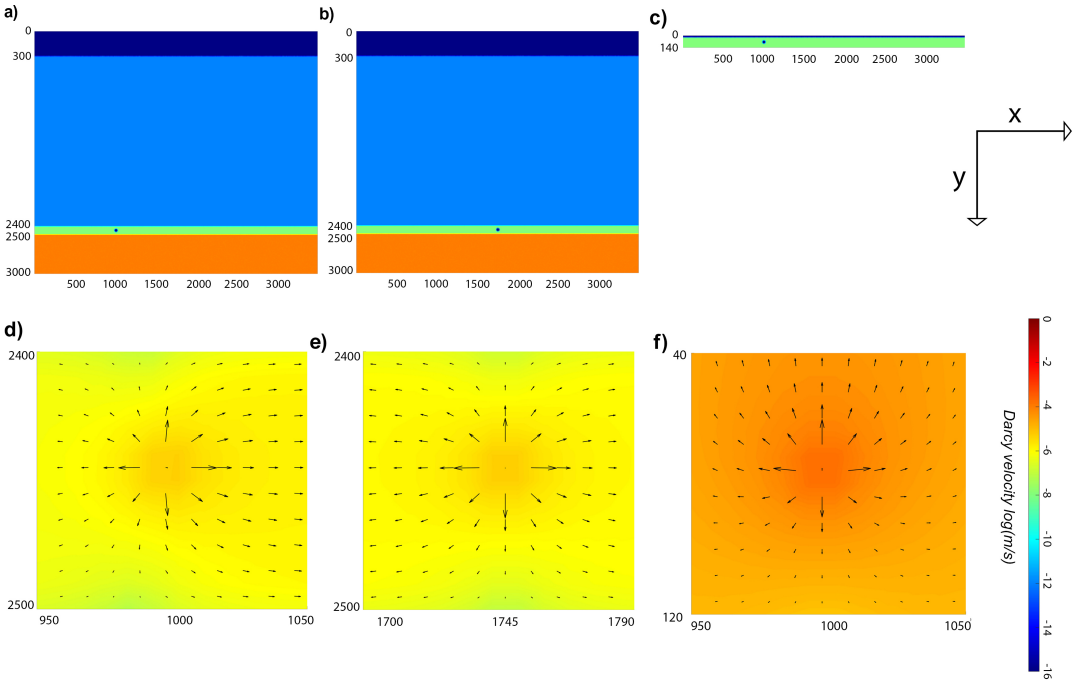

FIGURE 4.1: a) Base case 1 set-up, leading to an asymmetrical divergent fluid velocity field around the injection well, with a stronger rightward motion (d). b) An alternative model set-up with an injection well is placed at the center of the reservoir, leading to a symmetrical divergent Darcy velocity field (e). c) An alternative model set-up without an over- or under-burden, yielding a divergent Darcy velocity field with a stronger upward motion: f. The background in d,e, and f is the magnitude of the Darcy velocity vectors (black arrows).

4.1.2 Velocity acceleration events

Two peaks in the solid velocity can be distinguished in figure 4.2. The first event occurs after 283 days of injection and lasts roughly an hour (figure 4.3). Increased velocities and stress are recorded as the strain accumulates (figure 4.3). The total pressure drops simultaneously to this, while there is no disturbance in the fluid pressure, meaning the drop in total pressure is entirely due to a drop in solid pressure. As the accumulated strain is released the velocity decreases and the total pressure slowly increases, but no drop is found in the stress. The plastic-yielding conditions are not met during this event and there is no clear source for the event. Rather, an instantaneous increase in the second invariant of the strain rate is found throughout the entire model.

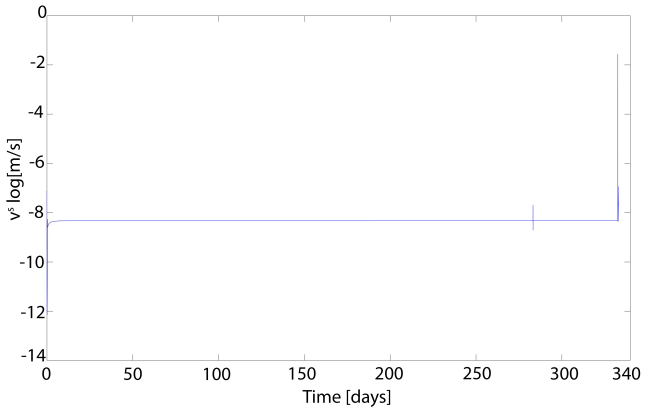

FIGURE 4.2: Two peaks are found in the magnitude of the solid velocity field at the location of the injection well.

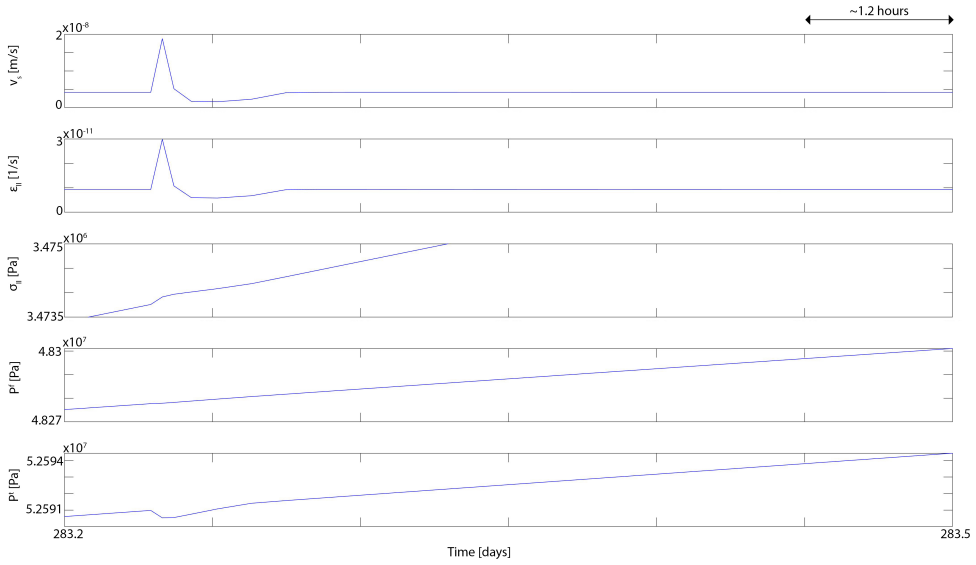

FIGURE 4.3: Zoom-in of parameter changes during the first velocity acceleration event. From top to bottom: the solid velocity magnitude, the second invariant of the strain rate, the second invariant of the stress tensor, the fluid pressure, and the total pressure during the first velocity acceleration event.

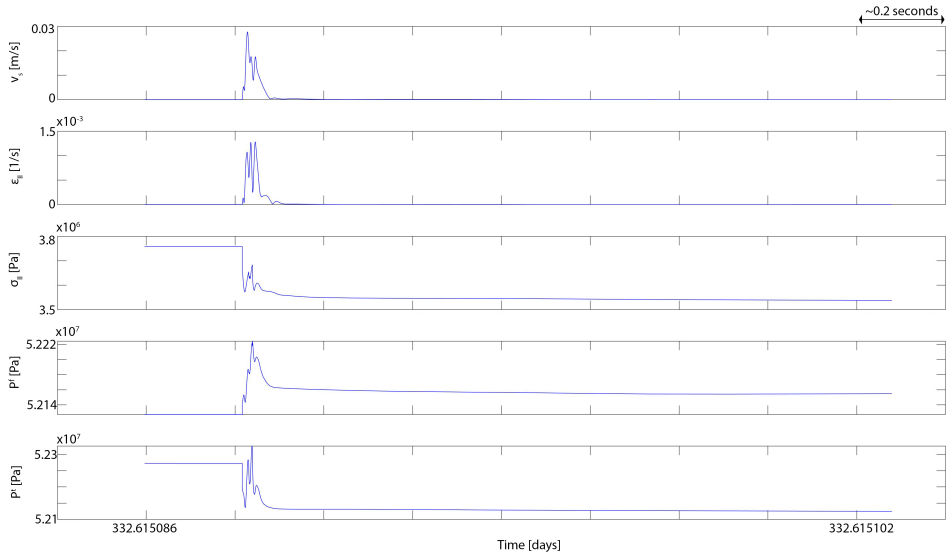

FIGURE 4.4: Zoom-in of parameter changes during the second velocity acceleration event. From top to bottom: the solid velocity magnitude, the second invariant of the strain rate, a 0.2 MPa drop in the second invariant of the stress tensor, the fluid pressure, and a 0.2 MPa drop in the total pressure during the second velocity acceleration event.

The second event, which is made up out or a cluster of events, occurs after 332 days (figure 4.4). The highest velocity is in the order of magnitude of cm/s, which is typical for dynamic rupture propagation (e.g. Gerya (2019)). The seismic moment that is generated is 2e11 Nm, which translates to a local magnitude (M_L) of 1.5. The event comes to rest after 1s, which allows for the identification and investigation of different stages of the seismic cycle: 1) inter-seismic (figure 4.5), 2) nucleation (co-seismic) (figure 4.6), 3) propagation (co-seismic) (figure 4.7), and 4) post-seismic (figure 4.8).

Resolving the yielding conditions requires a lot of iterations, which slowed down the model substantially: 31 days of computation were required to bring the rupture to arrest (1s of model time), as opposed to the 25 days that were required to model everything up to the moment of rupture (332 days in model time).

Inter-seismic period

Uniform strain rates ($10^{-8}s^{-1}$) and velocities ($10^{-5}m/s$) are found in and around the reservoir during this period (figure 4.5). A peak in the elastic decompaction rates ($10^{-8}s^{-1}$) is found at the upper boundary of the reservoir, this means the fluid pressure is increasing more rapidly at this location than the total pressure (figure 4.5). At this same location, the yielding stress and second invariant of the stress tensor are virtually equal to one another (figure 4.5).

Nucleation

The plastic yielding conditions are met for tensile fractures (equation 3.31) at the top boundary of the reservoir at the moment of nucleation, resulting in an instantaneous stress drop (figure 4.6). A drop of 0.2 MPa is found in the second invariant of the

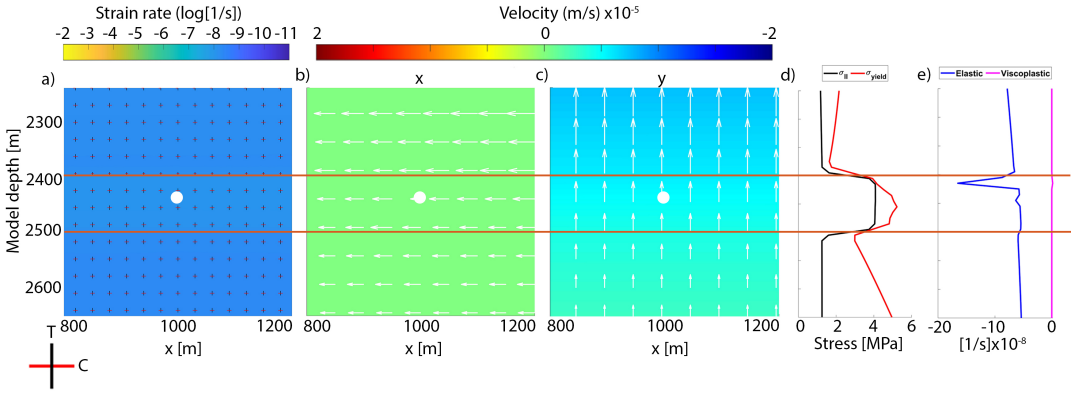

FIGURE 4.5: The inter-seismic period of the second velocity acceleration event in and around the reservoir (red lines) and injection well (white dots). The axes of maximum compressive stress (red) and maximum tensile stress (black) are horizontal and vertical throughout the model. a) the total strain rate, b) the x component of the solid velocity, c) the y component of the solid velocity, d) the second invariant of the stress tensor (black) and the yielding stress (red) along the line x=$x_{injectionwell}$, d) the elastic (blue) and viscoplastic (magenta) (de)compaction rates along the line x=$x_{injectionwell}$.

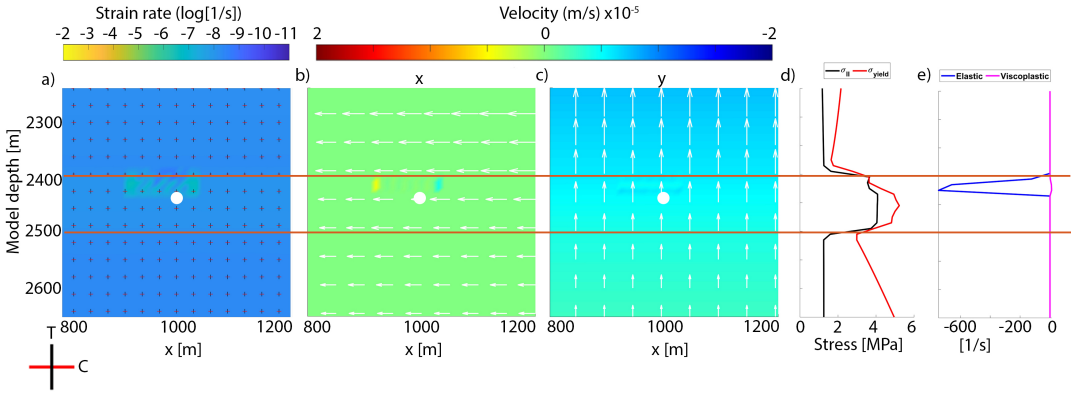

FIGURE 4.6: The nucleation of the second velocity acceleration event in and around the reservoir (red lines) and injection well (white dots). The axes of maximum compressive stress (red) and maximum tensile stress (black) are horizontal and vertical throughout the model. a) the total strain rate, b) the x component of the solid velocity, c) the y component of the solid velocity, d) the second invariant of the stress tensor (black) and the yielding stress (red) along the line x=$x_{injectionwell}$, d) the elastic (blue) and viscoplastic (magenta) (de)compaction rates along the line x=$x_{injectionwell}$.

stress tensor, as well as the total pressure (figure 4.4), while the fluid pressure keeps rising, leading to very high elastic decompaction rates ($10^2 s^{-1}$) between the well and the upper reservoir boundary (figure 4.6). This area is furthermore met with slightly elevated strain rates ($10^{-6} s^{-1}$) and velocities (figure 4.6).

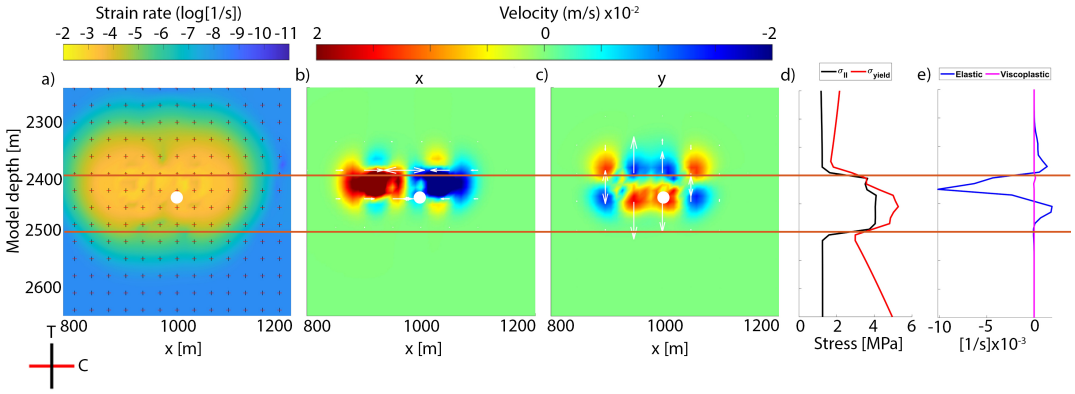

FIGURE 4.7: The propagation of the second velocity acceleration event in and around the reservoir (red lines) and injection well (white dots). The axes of maximum compressive stress (red) and maximum tensile stress (black) are horizontal and vertical throughout the model. a) the total strain rate, b) the x component of the solid velocity, c) the y component of the solid velocity, d) the second invariant of the stress tensor (black) and the yielding stress (red) along the line x=$x_{injectionwell}$, d) the elastic (blue) and viscoplastic (magenta) (de)compaction rates along the line x=$x_{injectionwell}$.

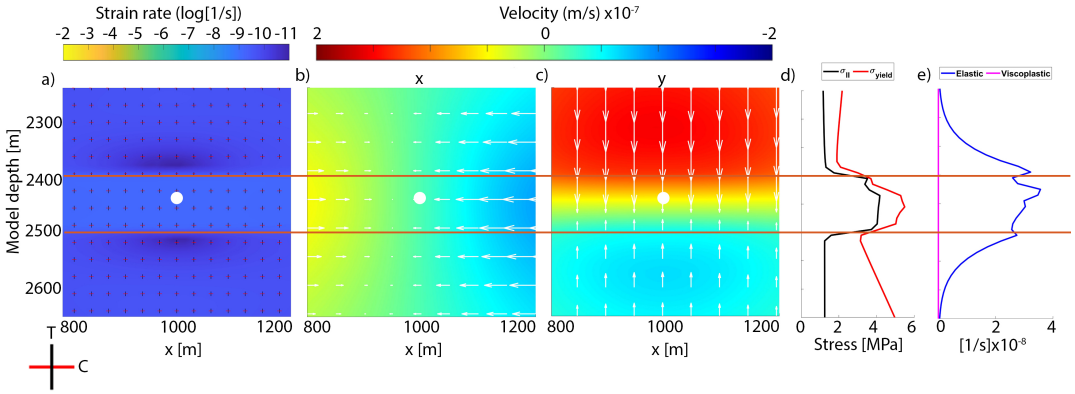

FIGURE 4.8: The post-seismic period of the second velocity acceleration event in and around the reservoir (red lines) and injection well (white dots). The axes of maximum compressive stress (red) and maximum tensile stress (black) are horizontal and vertical throughout the model. a) the total strain rate, b) the x component of the solid velocity, c) the y component of the solid velocity, d) the second invariant of the stress tensor (black) and the yielding stress (red) along the line x=$x_{injectionwell}$, d) the elastic (blue) and viscoplastic (magenta) (de)compaction rates along the line x=$x_{injectionwell}$.

Propagation

The propagating waves reach the order of magnitude of cm/s, with strong compressive x-components (figures 4.4 and 4.7). Compressive y-components are found on the outside of the nucleus, with tensile motions towards the center. The maximum compressive stress axis remains horizontal (figure 4.7).

The area of increased strain is propagating radially and elevated strains are now

also found in the over- and under-burden (figures 4.7). The rate of elastic decompaction has decreased ($10^{-3}s^{-1}$) at the top boundary of the reservoir (figure 4.7). Elastic compaction is now found in the overburden at the boundary with the reservoir as well as within the reservoir at the lower boundary, implying that fluid is being released from the pores in these areas (figure 4.7).

Post-seismic period

The accumulated strain has been released at this moment and the yielding conditions are no longer being met (figure 4.8). The x-components of the velocity field, which have decreased to $\pm 10^{-7}$ m/s, are still oriented in a compressive motion, while the y-components now fully have a compressive orientation, with a stronger downward motion (figure 4.8). Finally, elastic compaction is found throughout the depicted area, suggesting that fluid is being released from the pores (figure 4.8). No difference was recorded between the porosity before and after the event.

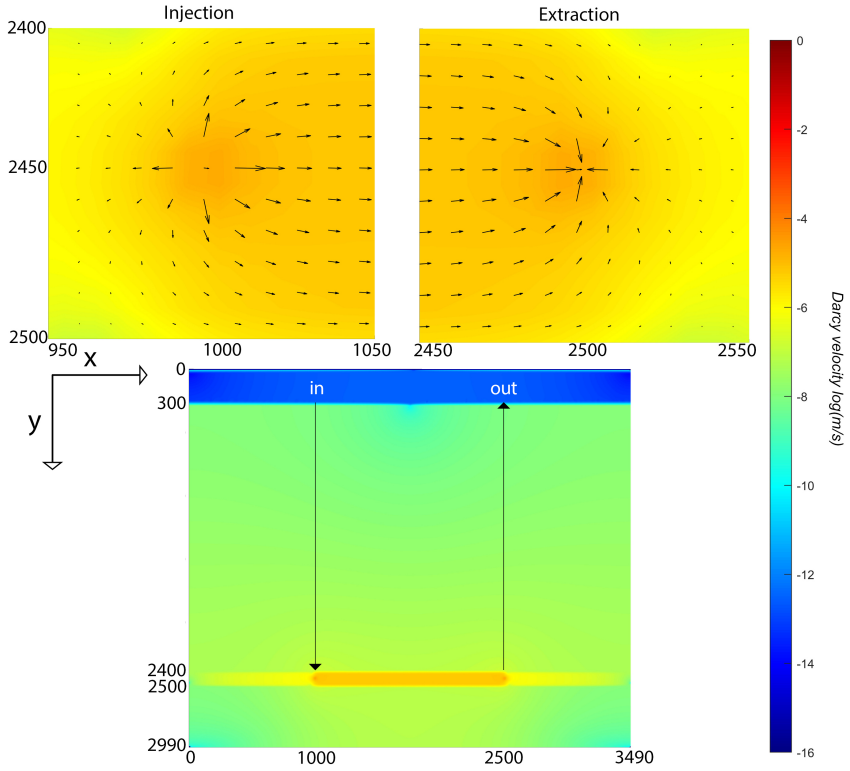

FIGURE 4.9: The magnitude of the velocity vectors (black arrows) around the injection well (top left), the production well (top right), and throughout the entire model domain (bottom).

4.2 Base case 2: doublet model

Higher fluid velocities are found in the reservoir due to the addition of the production well, in comparison to base case one (figure 4.1). On a large scale, the fluid-velocity field that has been created due to injection and production is symmetrical, with the highest velocities restricted to the reservoir and three points of slowed fluid flow found at: the bottom right corner, the bottom left corner, and at the center of the model below the sticky-air (figure 4.9). A divergent velocity field is still found around the injection well, although the x-component to the right has become stronger (with respect to base case 1) due to the presence of the production well, which has created a convergent velocity field. The highest velocities are found between the wells (figure 4.9).

Starting at 115 days an instability is found in the x- and y-components of the solid velocity (figure 4.10). This same instability is found in the second invariant of the strain rate (figure 4.10). However, it is not found in the second invariant of the stress tensor, nor is it found in the fluid pressure or the total pressure. The instability is found in all other models with a doublet system (base case 3 and all the models for the parameter study), therefore only the first 100 days of the results will be presented in this thesis.

In 100 days less fluid pressure has accumulated around the injection well than for base case 1- although the difference is minimal- while there is virtually no difference in the total pressure (figure 4.11). Therefore, the yielding stress is slightly larger, as the effective pressure is larger. Less stress has built up around the injection well, with respect to base case 1. Minimal differences are found between the strain rates found in base cases 1 and 2.

100 days of fluid extraction from the production has resulted in a substantiallt less high fluid pressures along the line $x = x_{injectionwell}$ (compared to base case 1) with the lowest pressures found at the top of the reservoir (figure 4.12). A higher yielding stress is found at the production well than at the injection well, due to the fact that the effective pressure is higher. The second invariant of the stress tensor is substantially smaller than in base case 1 but equal to the stress found in the injection well, meaning that the stress build-up is less localized (with respect to base case 1) due to the production well. Furthermore, the strain rates that are found at the production well are similar to those found at the injection well.

A less uniform stress field is found around the injection well (figure 4.13), with respect to base case 1 (e.g. figure 4.5.a). In base case 1 the axis of maximum compression was horizontal throughout the entire model domain. In this model the axis of maximum compression varies, within the reservoir it is almost horizontal (with a slight anti-clockwise rotation) (figure 4.13). Furthermore, the axis of maximum compression is almost vertical in the under-burden. This is mirrored at the production well: vertical maximum compressive stress in the reservoir and horizontal maximum compressive stress in the under-burden (figure 4.13).

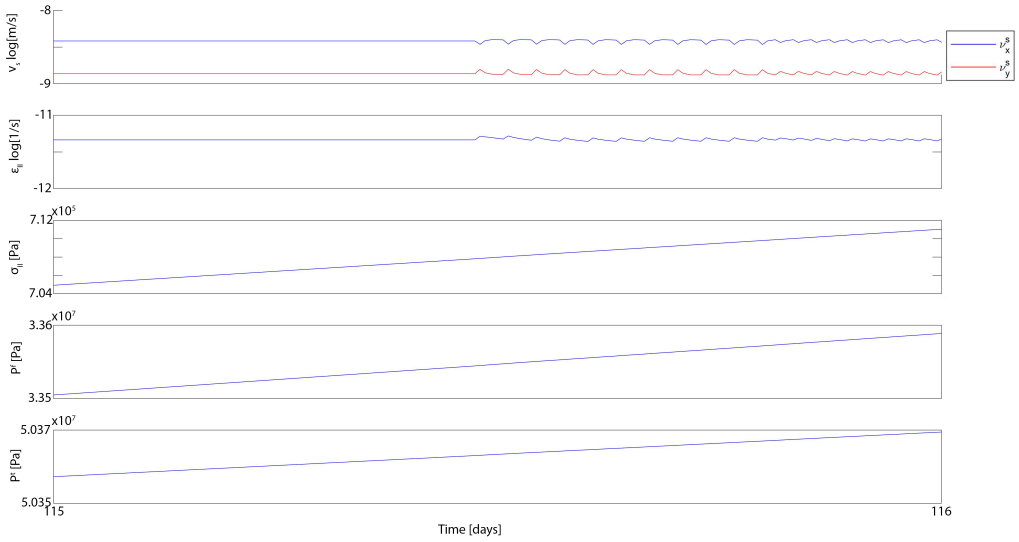

FIGURE 4.10: From top to bottom: 1) an instability is found in the velocity (log-scale) after 115.5 days,2) which affects the second invariant of the strain rate (log-scale), 3) the second invariant of the stress tensor, 4) fluid pressure, and 5) total pressure seem unaffected.

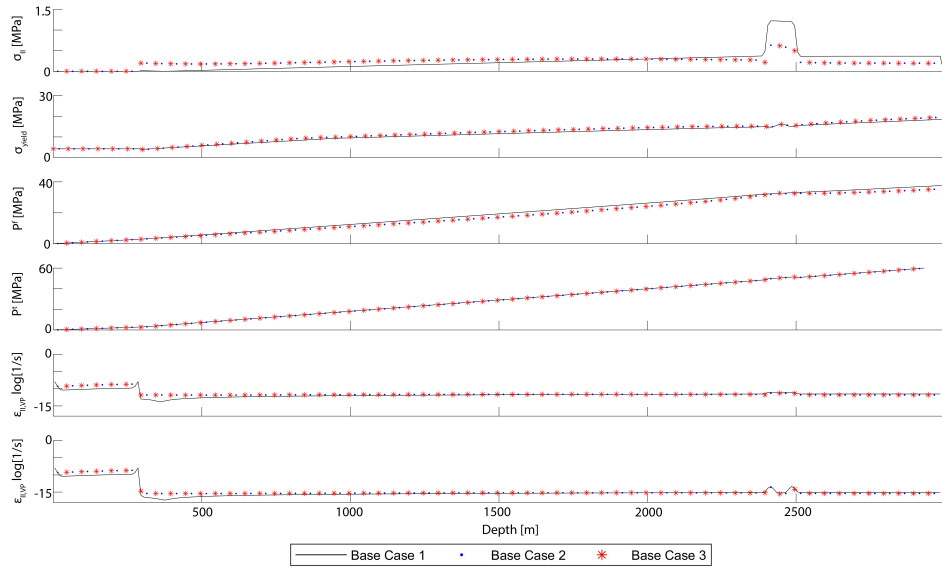

FIGURE 4.11: A comparison of the base cases along the line $x = x_{injectionwell}$ after 100 days. From top to bottom: 1) less stress has accumulated in the reservoir for base cases 2 and 3, 2) slightly higher yielding stress is found along this line for base cases 2 and 3, 3) lower fluid pressures are found along the line for base cases 2 and 3, 4) no difference in the total pressure is found along the line, 5) higher strain rates are found in the sticky air and just below the sticky air for base cases 2 and 3, 6) higher visco-plastic strain rates are found in the sticky air and just below the sticky air for base cases 2 and 3.

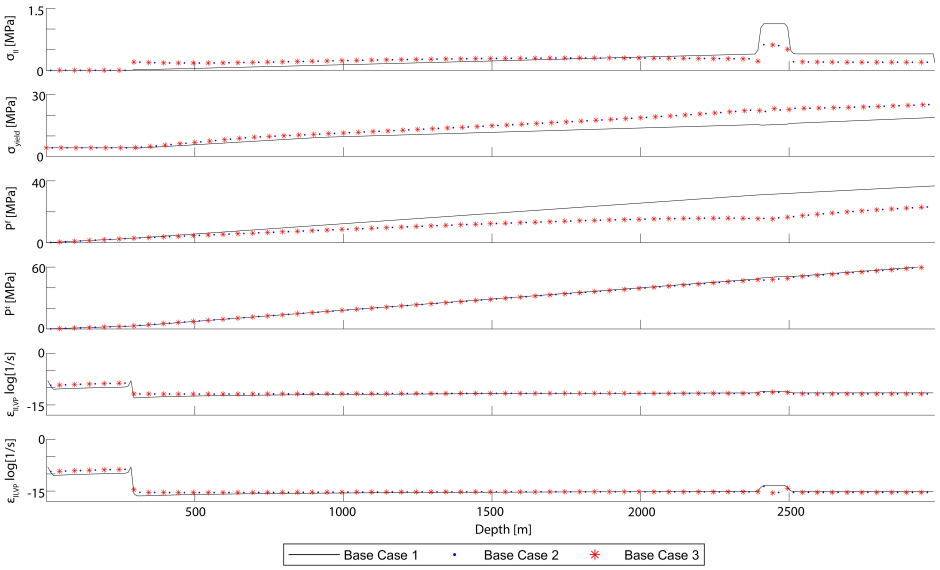

FIGURE 4.12: A comparison of the base cases along the line $x = x_{productionwell}$ after 100 days. From top to bottom: 1) less stress has accumulated in the reservoir as well as in the under-burden, for base cases 2 and 3, 2) substantially higher yielding stress is found along this line for base cases 2 and 3, 3) lower fluid pressures are found along the line for base cases 2 and 3, 4) no difference in the total pressure is found along the line, 5) no difference is found in the strain rate along this line, 6) a lower visco-plastic strain rate is found in the reservoir for base cases 2 and 3.

4.3 Base case 3: doublet model with fault

On a large scale, the results for base case 3 are identical to those in base case 2: the fault does not have an influence on the fluid velocity field (figure 4.14), the same instability is found in the velocity (figure 4.15), no difference is found in the strain rates, the stress field (figure 4.13), and pressures around the injection (figure 4.11) and production well (figure 4.12). Furthermore, when the fault is studied in more detail after 100 days, no difference can be noticed between the faulted (base case 3) and the un-faulted situation (base case 2), not even in the yielding stress (figure 4.16).

4.4 Parameter study

4.4.1 Pressure rates

Smaller time steps were required for rates larger than ± 1 Pa/s. The models that used these rates, therefore, were not able to run long enough to reach 100 days. Solving the equations takes increasingly more time for higher rates: 65 days were required to model 3.8 days for the model that used ± 100 Pa/s of fluid injection as opposed to 11 days that were required to model 100 days for base case 3.

2 days of injecting and extracting fluids has not yet influenced the total or fluid pressure (and thus also not the yielding stress) within the fault (figure B.1). Yet the stress that has accumulated on the fault is 0.5 MPa larger for the model that used a rate of ± 100 Pa/s than the other models, with the highest stresses found within

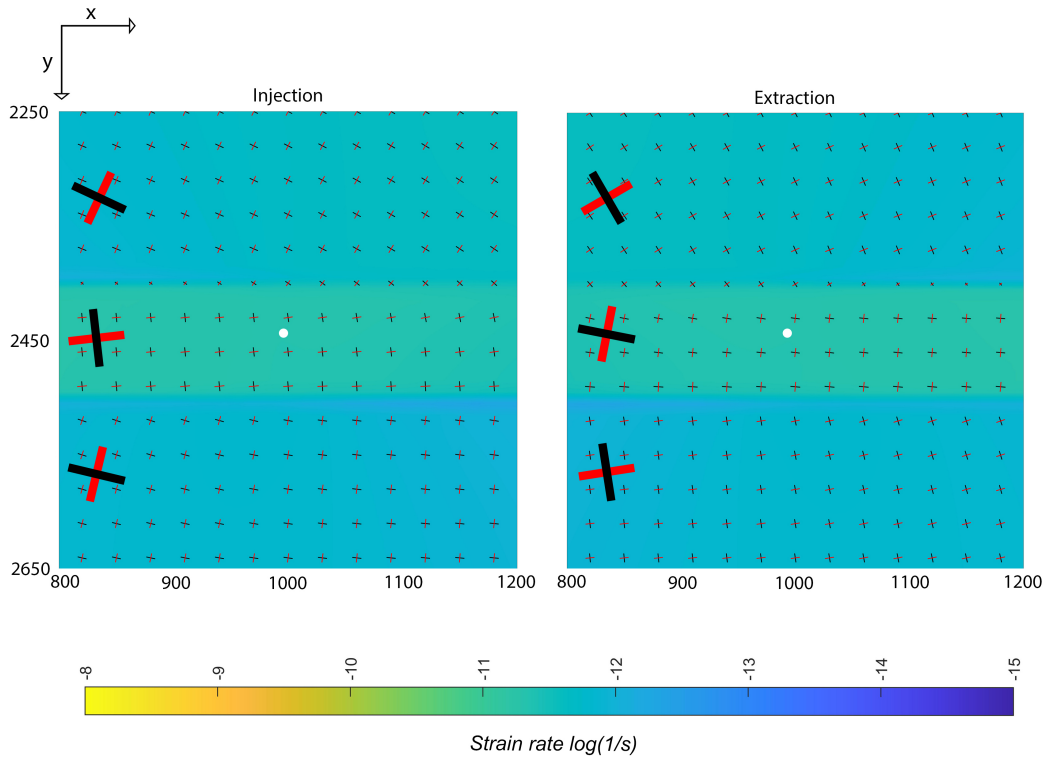

FIGURE 4.13: The magnitude of the second invariant of the strain rate (log-scale) with the orientation of the stress axes: red for compression and black for extension. The white dots are the injection (left) and extraction (right) points.

the over-burden (figure B.1). Furthermore, higher strain rates are found for higher pressure rates and lower strain rates for lower pressure rates, throughout the entire model (figure B.1).

4.4.2 Fault parameters

The studied properties (second invariant of the stress tensor, yielding stress, total pressure, fluid pressure, or the strain rates) are influenced less harshly during the fault parameter studies (figures B.2-B.5). Increasing the fault throw results in higher stresses at the depth of the reservoir, with slightly lower yielding stress at the same depth (figure B.2). However, the other properties seem not to be influenced. No noticeable differences are found in the studied properties along the fault after 100 days during the permeability, porosity, and strength tests (figures B.3-B.5).

The velocity instability that was found for base cases 2 and 3 also arises in all models for the parameter study (although the start time varies), with the exception of the models with different pressure rates. No variation is found in the solid velocity for models with a lower pressure rate (i.e. 0.01 and 0.1 Pa/s), the velocities are also lower for these models (with respect to base case 3). The variations in the velocities for the models with higher pressure rates also include instabilities but include larger variations that seem to be related to clusters of events: the velocities are higher (figures 4.17 and 4.18), a nucleus is present, it corresponds with a stress drop(figures 4.17 and 4.18), and the plastic yielding conditions are met.

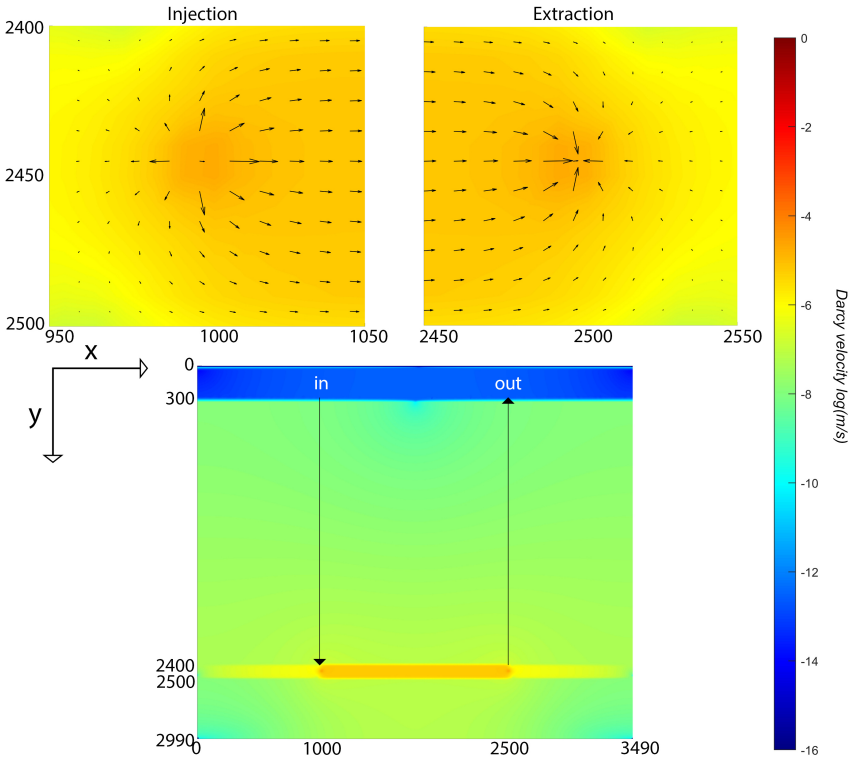

FIGURE 4.14: The magnitude of the velocity vectors (black arrows) around the injection well (top left), the production well (top right), and throughout the entire model domain (bottom), these results are identical to those from base case 2 (figure 4.9).

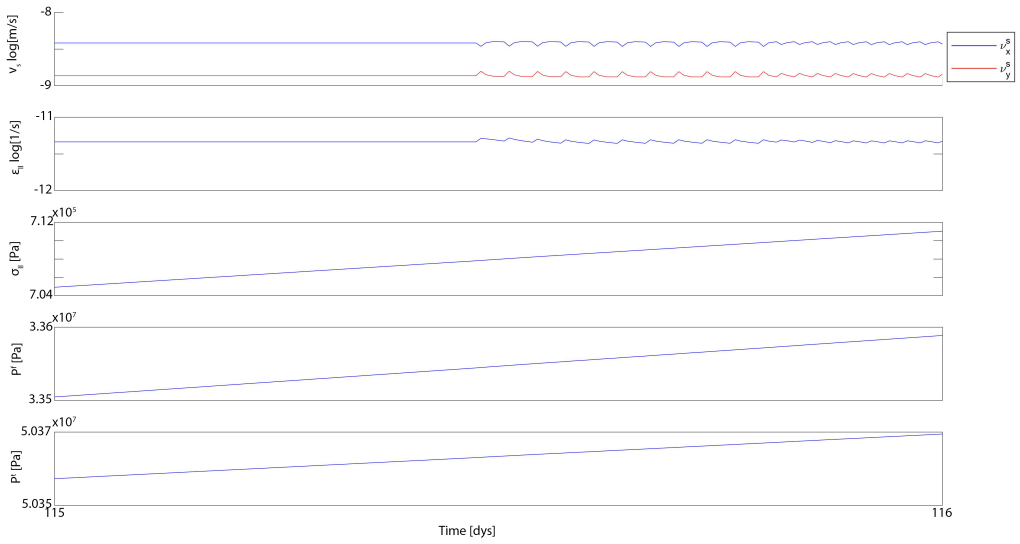

FIGURE 4.15: From top to bottom: 1) an instability is found in the velocity (log-scale) after 115.5 days,2) which affects the second invariant of the strain rate (log-scale), 3) the second invariant of the stress tensor, 4) fluid pressure, and 5) total pressure seem unaffected. These results are identical to those from base case 2 (figure 4.10).

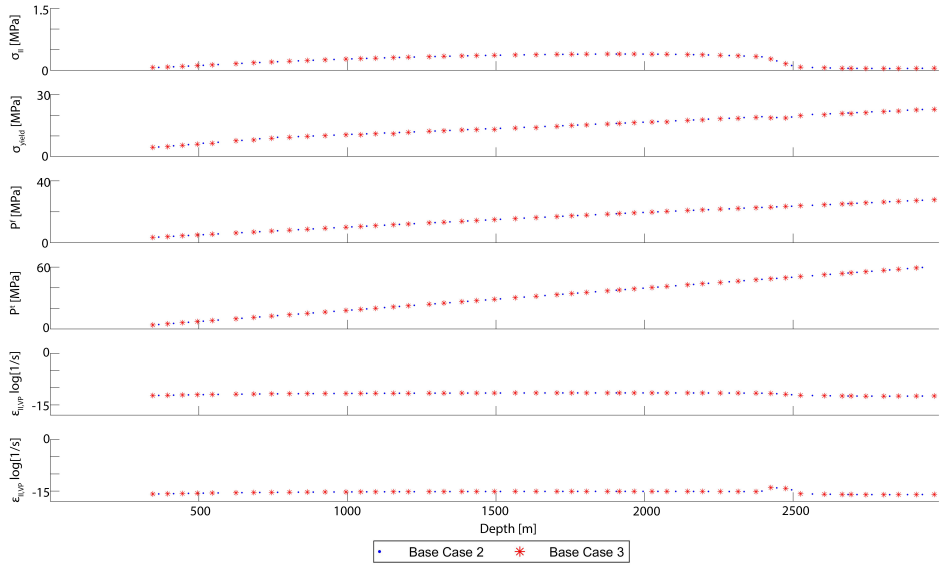

FIGURE 4.16: Comparison between base case 2 and 3 along the fault location after 100 days. No difference is found between the two base cases, from top to bottom: 1) the second invariant of the stress tensor, 2) the yielding stress, 3) the fluid pressure, 4) the total pressure, 5) the second invariant of the strain rate tensor, 6) the second invariant of the visco-plastic strain rate tensor.

4.4.3 Velocity acceleration events

The events that occur due to the higher injection and production rates nucleate within the over-burden at the lower boundary with the reservoir, where the yielding stress is the lowest (figures C.1 and C.4). The plastic-yielding conditions are met during the nucleation phase above the upper reservoir boundary (figures C.2 and C.5). Slightly elevated strain rates and velocities are found within the same area. The elevated strain propagates radially for the model with pressure rates of $\pm$100 Pa/s(figure C.6, while for the model with pressure rates of $\pm$10 Pa/s it propagates laterally along the boundary with the reservoir (figure C.3). These same radial and lateral patterns can be found in the velocity fields: the event that was triggered by $\pm$100 Pa/s results in velocity waves propagating away from the source (figure C.6), while the event that was caused due to $\pm$10 Pa/s shows an area of increased velocity migrating to the left (figure C.3).

Before the rupture, the elastic decompaction rates peak slightly above the upper boundary and slightly below the lower boundary of the reservoir for both models (figures C.1 and C.4). During the nucleation the reversible visco-plastic decompaction rates increase for the model with pressure rates of $\pm$10 Pa/s, suggesting that $P^f > P^t$ (equation 3.5, figures C.2). As the rupture progresses, elastic compaction is now occurring at the location of the rupture (figure C.3 and C.6).

The $\pm$100 Pa/s event generates a seismic moment of 2.2E4 Nm, while no seismic moment is recorded for the $\pm$10 Pa/s event. No noteworthy changes in porosity were recorded.

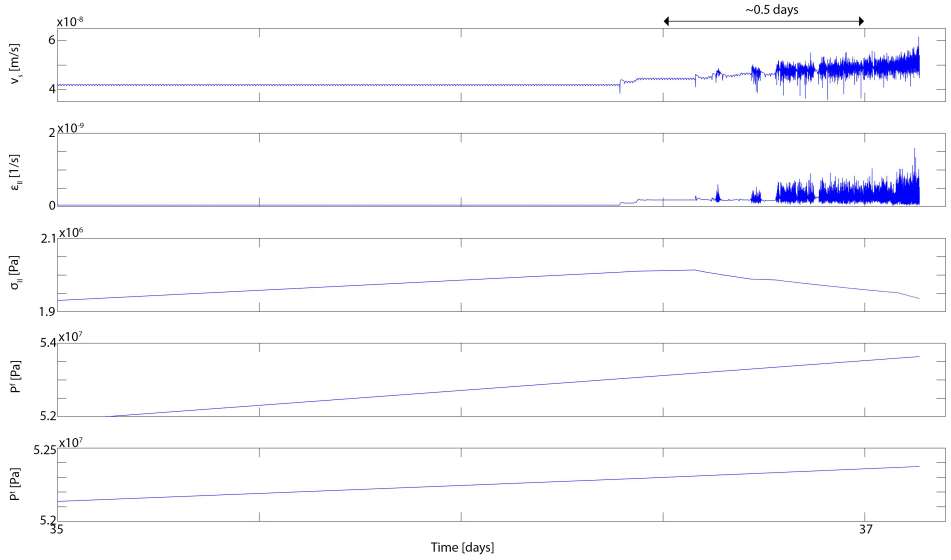

FIGURE 4.17: From top to bottom: 1) the solid velocity, 2) the second invariant of the strain rate tensor, 3) the second invariant of the stress tensor, 4) the fluid pressure, and 5) the total pressure. During the events induced by ± 10 Pa/s pressure rates

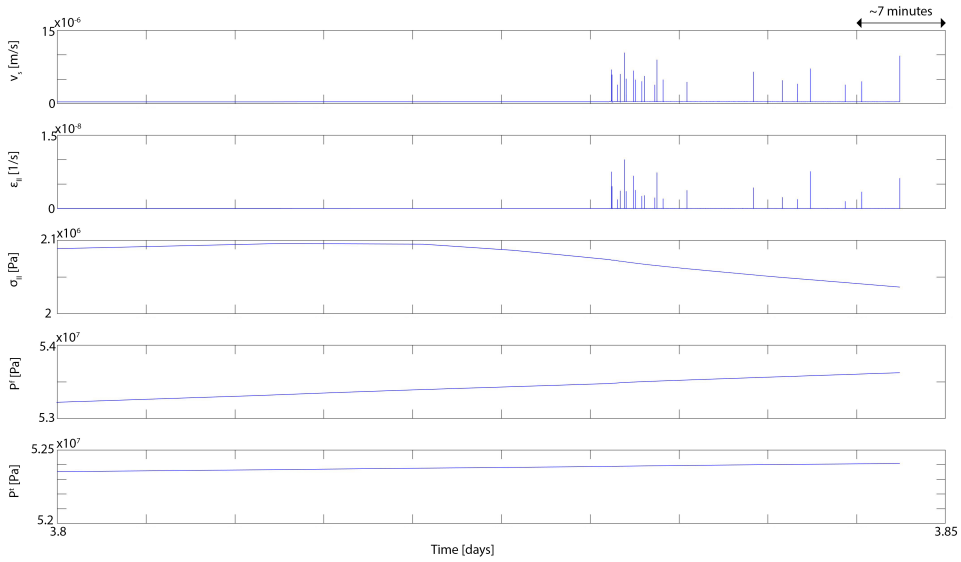

FIGURE 4.18: From top to bottom: 1) the solid velocity, 2) the second invariant of the strain rate tensor, 3) the second invariant of the stress tensor, 4) the fluid pressure, and 5) the total pressure. During the events induced by ± 100 Pa/s pressure rates

4.5 Errors found in the Petrini code

4.5.1 (De)compaction

While plotting the (de)compaction results a mistake was found in the coding of the porosity evolution (equation 3.5) and in the way the effective viscosity is coded (equation 3.13). The value that is stored as the effective viscosity (η^{φ}) is the shear

```
dxm=(xm(m)-xp(j))/dx;
dym=(ym(m)-yp(i))/dy;
% interpolating from the markers to the pressure node
    wtmij=(1-dxm)*(1-dym);
    ETAPSUM(i,j)=ETAPSUM(i,j)+etamm*wtmij;
    PORSUM(i,j)=PORSUM(i,j)+porm(m)*wtmij;
    SXXSUM(i,j)=SXXSUM(i,j)+sxxm(m)*wtmij;
    GGGPSUM(i,j)=GGGPSUM(i,j)+1/gm(m)*wtmij;
    ETAP0SUM(i,j)=ETAP0SUM(i,j)+etamm0*wtmij;
    ETAB0SUM(i,j)=ETAB0SUM(i,j)+etasmm0*wtmij;
    WTPSUM(i,j)=WTPSUM(i,j)+wtmij;

    wtmi1j=(1-dxm)*(dym);
    ETAPSUM(i+1,j)=ETAPSUM(i+1,j)+etamm*wtmi1j;
    PORSUM(i+1,j)=PORSUM(i+1,j)+porm(m)*wtmi1j;
    SXXSUM(i+1,j)=SXXSUM(i+1,j)+sxxm(m)*wtmi1j;
    GGGPSUM(i+1,j)=GGGPSUM(i+1,j)+1/gm(m)*wtmi1j;
    ETAP0SUM(i+1,j)=ETAP0SUM(i+1,j)+etamm0*wtmi1j;
    ETAB0SUM(i+1,j)=ETAB0SUM(i+1,j)+etasmm0*wtmi1j;
    WTPSUM(i+1,j)=WTPSUM(i+1,j)+wtmi1j;

    wtmij1=(dxm)*(1-dym);
    ETAPSUM(i,j+1)=ETAPSUM(i,j+1)+etamm*wtmij1;
    PORSUM(i,j+1)=PORSUM(i,j+1)+porm(m)*wtmij1;
    SXXSUM(i,j+1)=SXXSUM(i,j+1)+sxxm(m)*wtmij1;
    GGGPSUM(i,j+1)=GGGPSUM(i,j+1)+1/gm(m)*wtmij1;
    ETAP0SUM(i,j+1)=ETAP0SUM(i,j+1)+etamm0*wtmij1;
    ETAB0SUM(i,j+1)=ETAB0SUM(i,j+1)+etasmm0*wtmij1;
    WTPSUM(i,j+1)=WTPSUM(i,j+1)+wtmij1;

    wtmi1j1=(dxm)*(dym);
    ETAPSUM(i+1,j+1)=ETAPSUM(i+1,j+1)+etamm*wtmi1j1;
    PORSUM(i+1,j+1)=PORSUM(i+1,j+1)+porm(m)*wtmi1j1;
    SXXSUM(i+1,j+1)=SXXSUM(i+1,j+1)+sxxm(m)*wtmi1j1;
    GGGPSUM(i+1,j+1)=GGGPSUM(i+1,j+1)+1/gm(m)*wtmi1j1;
    ETAP0SUM(i+1,j+1)=ETAP0SUM(i+1,j+1)+etamm0*wtmi1j1;
    ETAB0SUM(i+1,j+1)=ETAB0SUM(i+1,j+1)+etasmm0*wtmi1j1;
    WTPSUM(i+1,j+1)=WTPSUM(i+1,j+1)+wtmi1j1;
```

FIGURE 4.19: ETAB0SUM is the sum of the η^{φ} stored on markers surrounding pressure node (i,j). The marker property that is being summed in ETAB0SUM is etasmm0 (η^0), which is 10^{-3} for the sticky air and 10^{21} for the rest of the model. This should be etamm0/porm(m), with etamm0 being the effective shear viscosity (η) on the marker and porm(m) the porosity (φ) on the same marker.

a)

```
%DPOR calculation, interpolating from the pressure nodes to the markers
divm1=((pt(i,j)-pf(i,j))/ETAP(i,j)+gggbkoef*(pt(i,j)-pf(i,j)-PTF0(i,j))/GGGP(i,j)/dt)*wtmij+...
        ((pt(i+1,j)-pf(i+1,j))/ETAP(i+1,j)+gggbkoef*(pt(i+1,j)-pf(i+1,j)-PTF0(i+1,j))/GGGP(i+1,j)/dt)*wtmi1j+...
        ((pt(i,j+1)-pf(i,j+1))/ETAP(i,j+1)+gggbkoef*(pt(i,j+1)-pf(i,j+1)-PTF0(i,j+1))/GGGP(i,j+1)/dt)*wtmij1+...
        ((pt(i+1,j+1)-pf(i+1,j+1))/ETAP(i+1,j+1)+gggbkoef*(pt(i+1,j+1)-pf(i+1,j+1)-PTF0(i+1,j+1))/GGGP(i+1,j+1)/dt)*wtmi1j1;


    % Porosity evolution
    A=(1-porm(m))/porm(m)*exp(divm1*dt);
    % Change in porosity
    porm(m)=1.0/(1.0+A);
```

b)

```
divm1=((pt(i,j)-pf(i,j))/(ETAB(i,j)*(1-POR(i,j))*POR(i,j))+gggbkoef*(pt(i,j)-pf(i,j)-PTF0(i,j))/(GGGB(i,j)*(1-POR(i,j))*POR(i,j)*dt))*wtmij+...
        ((pt(i+1,j)-pf(i+1,j))/(ETAB(i+1,j)*(1-POR(i+1,j))*POR(i+1,j))+gggbkoef*(pt(i+1,j)-pf(i+1,j)-PTF0(i+1,j))/(GGGB(i+1,j)*(1-POR(i+1,j))*POR(i+1,j)*dt))*wtmi1j+...
        ((pt(i,j+1)-pf(i,j+1))/(ETAB(i,j+1)*(1-POR(i,j+1))*POR(i,j+1))+gggbkoef*(pt(i,j+1)-pf(i,j+1)-PTF0(i,j+1))/(GGGB(i,j+1)*(1-POR(i,j+1))*POR(i,j+1)*dt))*wtmij1+...
        ((pt(i+1,j+1)-pf(i+1,j+1))/(ETAB(i+1,j+1)*(1-POR(i+1,j+1))*POR(i+1,j+1))+gggbkoef*(pt(i+1,j+1)-pf(i+1,j+1)-PTF0(i+1,j+1))/(GGGB(i+1,j+1)*(1-POR(i+1,j+1))*POR(i+1,j+1)*dt))*wtmi1j1;


    % Porosity evolution
    A=(1-porm(m))/porm(m)*exp(divm1*dt);
    % Change in porosity
    porm(m)=1.0/(1.0+A);
```

FIGURE 4.20: ETAP is the effective shear viscosity (η) on the pressure nodes, which is incorrectly being used to calculate divm ($\frac{D^s ln(\frac{1-\varphi}{\varphi})}{Dt}$ in a. b) is the suggested correction.

viscosity of solid rock grains (η^0), meaning that the effective viscosity that is used in the reservoir is 2 orders of magnitude too large (figure 4.19). This affects the visco-plastic compaction part ($\frac{P^t - P^f}{\eta^\varphi (1-\varphi)}$) of the mass conservation equations (equations 3.2 and 3.4): a too large value for the effective viscosity yields a smaller visco-plastic addition to these equations.

Furthermore, the porosity evolution is incorrectly calculated (figure 4.20.a). The effective shear viscosity and the shear modulus are used instead of the effective viscosity and the effective bulk modulus (respectively). The term $\varphi(1-\varphi)$ is also missing from the equation. This mistake was found to have a minimal effect on the (de)compaction of the pores.

4.5.2 Velocity instability

The velocity instability that first showed up in base cases 2 and 3 corresponds with instabilities found in the variable time step size (dt): a drop in dt overlaps with a drop in the maximum x-component, while a peak in the dt is found when the maximum x-component peaks (figure 4.21). The maximum x-component is used in one of the conditions to update the step size. If this condition is met and the step size is altered, extra iterations are executed, which have the purpose of lowering the velocities so that the condition is no longer met. Seismic events are resolved in this way. The largest x-component of the velocity, however, is found in the sticky air. The extra iterations result in lowered x-components throughout the rest of the model. Excluding the velocities in the sticky air (figure 4.22.a) results in stable velocities and strain rates (figure 4.22.b).

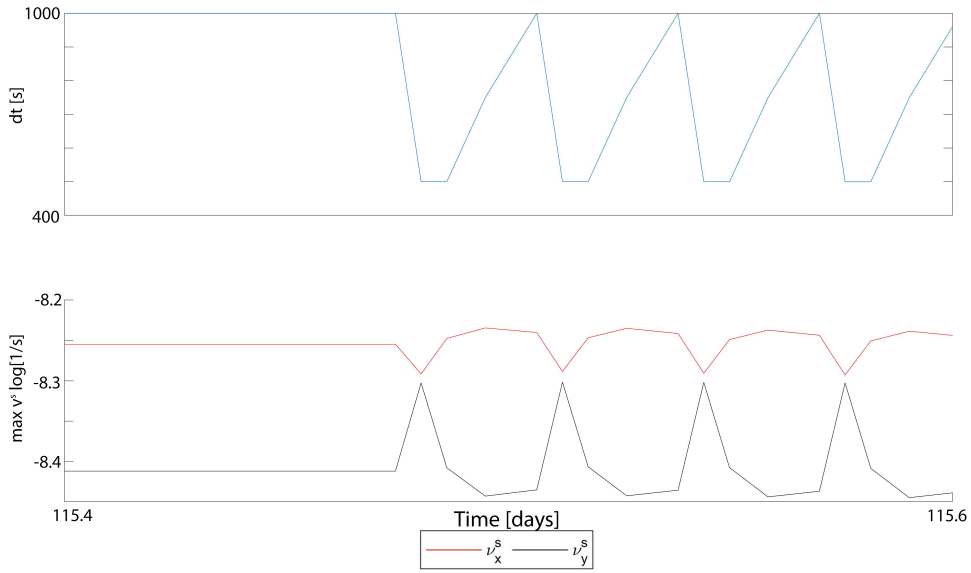

FIGURE 4.21: Visualisation of the relationship between the time step size (top) and the velocity (bottom).

a)

```
maxvxs=-1e+30;
minvxs=1e+30;
maxvys=-1e+30;
minvys=1e+30;
% Vx
for i=2:1:Ny
  for j=1:1:Nx
      if(yvx(i)>ysurface)%added
        maxvxs=max(maxvxs,abs(vxs(i,j)));
        minvxs=min(minvxs,abs(vxs(i,j)));
      end
  end
end
% Vy
for i=1:1:Ny
  for j=2:1:Nx
      if(yvy(i)>ysurface)%added
        maxvys= max(maxvys,abs(vys(i,j)));
        minvys=min(minvys,abs(vys(i,j)));
      end
  end
end

maxvxy=((maxvxs-minvxs)^2+(maxvys-minvys)^2)^0.5;

stpmaxcur=stpmax%/(maxvxy/veloc0)^velocpow
dtx=dt;

if(dt>dx*stpmaxcur/maxvxs)
%     dtx=dt/dtkoef;
    dtx=dx/dtkoefv*stpmaxcur/maxvxs
    yn=1;
end
```

b)

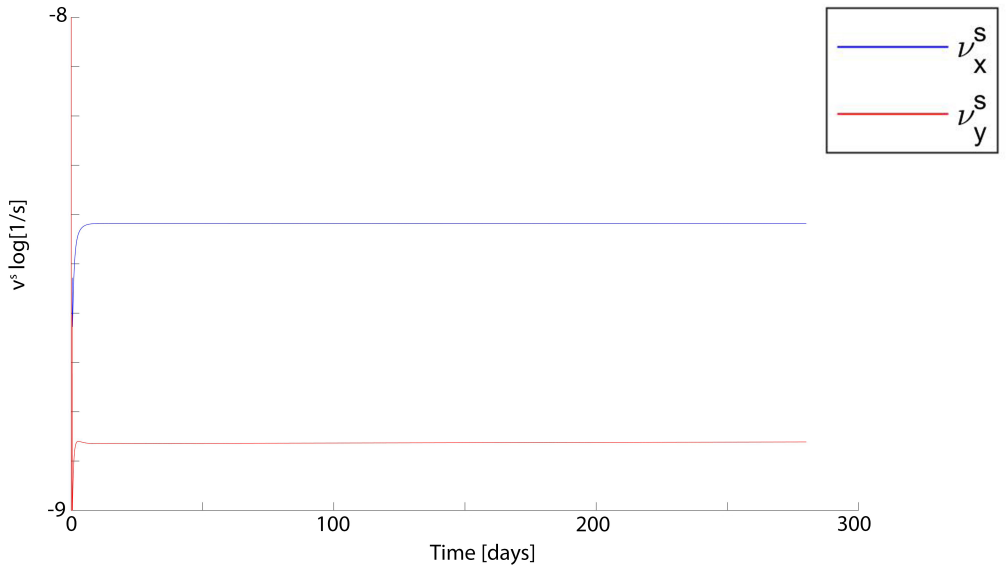

FIGURE 4.22: a) a suggested solution to solving the velocity instability, resulting in b) stable velocities

Chapter 5

Discussion

5.1 Velocity acceleration events

Multiple events have been modelled in an injection setting as well as a geothermal doublet setting. Despite the presence of the fault in the doublet settings, the events did not nucleate on the fault, suggesting that the presence of the fault is not required to trigger seismicity. This is in contrast with the general assumption that pre-existing (critically stressed) faults are necessary for inducing seismicity (e.g. Buijze et al. (2019) and Van Wees et al. (2014)). It could, however, be argued that the events that were triggered in the doublet setting are not actually seismic, considering the fact that the maximum recorded velocities are in the order of magnitude of $10^{-8} - 10^{-6}$ m/s (figures C.3 and C.6) and seismic propagation velocities are in the order of magnitude of $0.01 - 100$ m/s (Gerya (2019)).

It is important to note that the deformation events that occurred in the doublet setting, only occurred for models with higher injection and extraction pressure rates, which are rates that are not expected to be used in real life. For the rates that correspond better with real world injection and production rates, no seismicity was found in a doublet setting. It is possible that if these models had run for decades (model time), rather than a third of a year (model time), seismicity would have been triggered on the fault. Nevertheless, comparing base case 2 and 3 shows that imposing a weakness in the solid matrix has little effect on the yielding stress or the second invariant of the stress tensor, suggesting that with the current model parameters it is not more likely for deformation to occur on the fault.

This could be due to the way the fault was modelled. The imposed weakness was only prescribed on markers that occurred within the fault zone, which is thinner (1 m) than the model resolution (10x10 m). This method is effective in reflecting the heterogeneity of fault zones that can be found in nature, as the fault is not treated as a separate entity from the rest of the model. However, because the fault zone thickness is thinner than the resolution, the strength that is stored on the nodes and used in the rest of the calculations is much higher than the imposed, weakened strength. The effect of the fault zone thickness was not studied in this thesis, but it is advised to look into this in future work or to use a finer resolution around the fault.

The events that were generated by the ± 10 Pa/s and ± 100 Pa/s models were very similar to one another, but dissimilar from the event generated in base case 1. Firstly, the ± 10 Pa/s and ± 100 Pa/s events nucleate within the over-burden at the boundary with the reservoir, while the base case 1 event nucleates within the reservoir at the boundary with the over-burden. Secondly, while all events were generated due to the tensile plastic yielding conditions being met, the velocity field for base case 1 did not display tensile faulting, while the ± 10 Pa/s and ± 100 Pa/s models did. The deformation is in accordance with the orientation of the maximum

compressive and tensile stress axes: for base case 1 the axis of maximum compression is horizontal, while for the other two cases the axis of maximum compression is more vertical. These orientations are to be expected around the injection well: the pressurized well results in horizontal compression within the reservoir and vertical compression above and below (Buijze et al. (2019)). Lastly, irreversible visco-plastic (pore) decompaction does not occur during the base case 1 event but does for the ± 10 Pa/s and ± 100 Pa/s event.

The location of the nucleus always corresponded with the location where the fluid pressure was most rapidly increasing (with respect to the total pressure increase), resulting in peak elastic decompaction. This was always near the boundary between the over-burden and the reservoir (in the reservoir for the injection setting and in the over-burden for the geothermal models). A reason for this could be that the permeability and porosity are both lower within the over-burden, which leads to slower percolation of fluid, meaning the fluid pressure will increase more rapidly. The preliminary experiments (Appendix A) showed that this leads to a more localized increase in the strain rate.

Notably, there was no visible variation in the porosity during these events. Even when the total pressure dropped during the base case 1 event or when the fluid pressure started decreasing, the porosity within the reservoir remained unchanged. This can be attributed to the fact that the irreversible visco-plastic porosity compaction was always negligible in comparison to the reversible (de)compaction. This could, furthermore, be due to the fact that the solid and fluid mass conservation equations (equations 3.2 and 3.4) were incorrectly coded. However, the porosity evolution is calculated after the conservation equations are solved, so the pore (de)compaction is calculated based on the total and fluid pressure changes of the code and therefore can be trusted in reflecting the porosity evolution of the models (despite the error that was also found in this calculation, which is expected to have minimal consequences). The porosity variations may be simply too small to image.

5.2 Parameter study

Based on the results presented in the previous chapter, operational parameters (injection/production rates) have the greatest effect on the stress build-up around the well, on a short time scale (i.e. less than a year of production). This is due to the fact that the direct pressure effect (reducing the effective pressure by increasing the fluid pressure) is larger for larger injection rates.

The fault material parameters did not play an important role in the numerical experiments. This is in contrast with the finding that faults play a crucial part in inducing seismicity in real-life cases of induced seismicity due to geothermal operations (Buijze et al. (2019)). The fault parameters could potentially play a more important role on a longer timescale. Longer timescales (i.e. decades of production) allow for injected fluid to percolate throughout the model, resulting in drops in the effective pressure and poro-elastic stresses farther away from the well. The thermal stressing response was, furthermore, found to have a larger effect on the stress evolution of a fault by Buijze et al. (2019) and van Wees et al. (2020). More research into long-term geothermal operations and the effect of thermal stressing is advised to investigate this. To study the long-term effects of geothermal energy production, however, the model should be adapted to decrease the computational time.

5.3 Model time

All results shown in this thesis were produced by running the models for 1 to 2 months in real-time. The results with a doublet set-up (base cases 2 and 3, and the parameter study) were restricted to the first 100 (modeled) days of production, as a velocity instability was triggered, affecting parameters such as the strain rate. While the progression of the model in the presented modeled time offers great insights into how reservoirs evolve due to injection and extraction of fluids it can be considered too intricate (and therefore too slow) to view long-term effects. Considering the fact that induced seismicity in the Netherlands only started after decades of gas exploitation, it is also important to study the long-term effects of geothermal energy production.

Due to the increased complexity that plastic yielding adds to the code, the seismicity that was induced in the geothermal settings was not able to come to an arrest. A way to minimize the computational time during seismic events could be to assume solid and fluid incompressibility (Petrini et al. (2020)). This was proven to minimally affect the seismic behavior in a subduction zone setting, while decreasing the number of time steps required to resolve the co-seismic phase (Petrini et al. (2020)). Future work is advised to investigate if the incompressibility assumption affects the seismic behavior or the porosity evolution in a fluid injection/extraction setting and to see if this indeed results in a faster resolution of the co-seismic phase.

Another feature that slowed the model down was the velocity instability that was caused by the sticky air. More iterations are required than necessary to resolve an increase in the velocity that takes place in the boundary condition and therefore is not of interest. Neglecting the sticky air in the conditions for adapting the time step proves effective in solving this instability (figure 4.22), which decreases the computational time needed.

5.4 Effect of the boundary conditions

The free slip boundary conditions on all the boundaries (figure 3.2) are most likely responsible for the asymmetric fluid velocity field (figure 4.1). Due to these boundary conditions, fluid flows more freely from the injector into the direction that is farther away from the boundary. This is why a symmetric divergent pattern was found when the injection well was placed at the center of the reservoir (figure 4.1.e) and a stronger upward motion was recorded when the well was placed closer to the lower boundary (figure 4.1.f).

This could also be the reason why the fluid pressure increase is greater towards the upper reservoir boundary, while the permeability of the over- and under-burden is identical. The over-burden is larger and therefore offers more space between the reservoir and the upper boundary, allowing fluid to flow more freely towards the surface. However, this could also be due to the fact that due to the initial fluid pressure gradient, the fluid pressure is higher in the under-burden: fluid will flow with more ease to where the pressure is lowest.

Perhaps this has affected the location of the seismic nuclei. The three seismic events that were triggered all had a nucleus to the left and upward from the well, possibly this is due to the fact that fluid pressures are rising here, but due to the boundary conditions the fluid cannot flow away as fast as it should. More research is required to test this hypothesis: examining a model with an equally thick over- and under-burden with an injection well at the center of the reservoir could be used

to examine if a seismic event is triggered at the same location, relative to the injection well.

5.5 Implications for the Netherlands

On a short time scale, low injection and production rates are not sufficient in inducing seismicity in a geothermal reservoir that is based on the Dutch subsurface. The event that was triggered by injecting fluid at an estimated pressure rate based on the production rates used in the Netherlands (1.0 Pa/s), was of such a low magnitude (M_L = 1.5) that it would not classify as 'felt seismicity' (>2.0, Buijze et al. (2019)). Due to the presence of a production well the net pressure changes in the reservoir are smaller, leading to less stress being built up.

More research is advised to investigate the long-term effects of geothermal operations in the Dutch subsurface. Furthermore, it is recommended to incorporate temperature into the code in order to closely examine the effect of thermal stressing in the reservoir and in the fault, as this is expected to have a significant influence (Buijze et al. (2019) and van Wees et al. (2020)). Testing the stress evolution after production has ended is also important to consider as fluid percolation will continue and could therefore result in significant stress changes.

Chapter 6

Conclusion

The seismo-hydro-mechanical numerical model that was used in this thesis offers valuable insight into the stress and strain evolution of geothermal reservoirs due to fluid flow. It is successful in inducing localized events and bringing them to arrest, offering a greater understanding into how these events nucleate and propagate.

The injection and extraction rates play an important role in short-term stress effects. The two highest tested rates resulted in the only events triggered in a doublet system. These events were so small that they cannot be expected to be felt at the earth's surface.

The predefined fault did not play any role in inducing seismicity in the numerical experiments despite the fact that in real-life cases of induced seismicity, the presence of a fault is considered of great importance. This can be attributed to three potential reasons: 1) a longer run-time is required to investigate the effect of the fault, 2) the model resolution was ineffective to model the fault accurately, and 3) thermo-elastic stresses affect the fault more strongly. More research is required to investigate the effect of long-term geothermal operations on the stress evolution of faults.

While some errors were successfully corrected before the experiments that were presented in this thesis, the results showed that more improvements can be made to the code: 1) correctly defining the effective viscosity (η^{ϕ}) 2) correctly calculating the porosity evolution, and 3) neglecting the sticky air for any conditions for adapting the time step size. Furthermore, if this code is used for future work it is recommended to either adapt the velocity boundary conditions or to enlarge the model domain so that these conditions no longer have an effect on the velocity fields. Finally, in order to reduce the computational time in future work it is advised to assume solid and fluid incompressibility.

Chapter 7

Acknowledgements

In this final phase of my master's degree, I would like to take a moment to express my gratitude to a number of people who made this possible.

Firstly, I would like to thank my supervisors **Dr. Ylona van Dinther** and **Dr. Fred Beekman**. Thank you Ylona for entrusting me with this amazing project and for all your guidance. I learned so much from you these past years and I am extremely grateful that you took me under your wing. Thank you both for taking the time to give me in-depth feedback at various stages of the project, and helping me produce the best possible version of this thesis. Furthermore, I would also like to thank **Claudio Petrini**, for giving me access to his code, without which this project simply would not exist. Finally, I would like to thank **Mohsen Goudarzi** who helped set up this project.

I would also like to express my gratitude to my friends and family for all their moral support during a stressful time. Special thanks to my big sisters, **Elise** and **Lotte**, who have always been the best role models I could ask for not only as women in STEM but in every aspect of my life.

My most sincere thanks and appreciation to all of you,

Lynn Vogel

Bibliography

Biot, M. A. (1941). General theory of three-dimensional consolidation. *Journal of Applied Physics*, *12*(2), 155–164. https://doi.org/10.1063/1.1712886

Biot, M. A. (1955). Theory of elasticity and consolidation for a porous anisotropic solid. *Journal of Applied Physics*, *26*(2), 182–185. https://doi.org/10.1063/1.1721956

Biot, M. A. (1956a). General Solutions of the Equations of Elasticity and Consolidation for a Porous Material. *Journal of Applied Mechanics*, *23*(1), 91–96. https://doi.org/10.1115/1.4011213

Biot, M. A. (1956b). Theory of propagation of elastic waves in a fluid-saturated porous solid. ii. higher frequency range. *The Journal of the Acoustical Society of America*, *28*(2), 179–191. https://doi.org/10.1121/1.1908241

Boxem, T., Veldkamp, J., & van Wees, J. (2016). Ultra-diepe geothermie: Overzicht, inzicht to-do ondergrond. *TNO-rapport*.

Breede, K., Dzebisashvili, K., & Falcone, G. (2015). Overcoming challenges in the classification of deep geothermal potential. *Geothermal Energy Science*, *3*, 19–39.

Buijze, L., Bijsterveldt, L., Cremer, H., Jaarsma, B., Paap, B., Veldkamp, J., Wassing, B., Van Wees, J., van Yperen, G., & ter Heege, J. (2019). Induced seismicity in geothermal systems: Occurrences worldwide and implications for the netherlands. *Conference: European Geothermal Congress 2019*.

Buijze, L., van den Bogert, P.A.J., W., B.B.T., Orlic, B., & ten Veen, J. (2017). Fault reactivation mechanisms and dynamic rupture modelling of depletion-induced seismic events in a rotliegen gas reservoir. *Netherlands Journal of Geosciences*, *96*(5). https://doi.org/10.1017/njg.2017.27

Drucker, D., & Prager, W. (1952). Soil mechanics and plastic analysis or limit design. *Quarterly of Applied Mathematics*, *10*, 157–165.

Gerya, T. (2019). *Introduction to numerical geodynamic modelling*. Cambridge University Press.

Li, S., Feng, X.-T., Zhang, D., & Tang, H. (2019). Coupled thermo-hydro-mechanical analysis of stimulation and production for fractured geothermal reservoirs. *Applied Energy*, *247*, 40–59. https://doi.org/https://doi.org/10.1016/j.apenergy.2019.04.036

Mijnlieff, H. (2020). Introduction to the geothermal play and reservoir geology of the netherlands. *Netherlands Journal of Geosciences*, *99*(e2). https://doi.org/10.1017/njg.2020.2

Ministry of Economic Affairs and Climate Policy (MEA). (2022). Natural resources and geothermal energy in the netherlands. *Annual review*, *2021 annual review*, 0—174.

Moeck, I. S. (2014). Catalog of geothermal play types based on geologic controls. *Renewable and Sustainable Energy Reviews*, *37*, 867–882. https://doi.org/10.1016/j.rser.2014.05.032

Petrini, C. (2019). Fluid controls on subduction thrust seismicity: Seismo-hydro-mechanical modelling combined with experimental studies [doctoral dissertation, eth zurich]. *Swiss Federal Institute of Technology in Zürich*.

Petrini, C., Gerya, T., Yarushina, V., van Dinter, Y., Connolly, J., & Madonna, C. (2020). Seismo-hydro-mechanical modelling of the seismic cycle: Methodology and implications for subduction zone seismicity. *Tectonophysics*, *791*(228504). https://doi.org/10.1016/j.tecto.2020.228504

Rathnaweera, T. D., Wu, W., Ji, Y., & Gamage, R. P. (2020). Understanding injection-induced seismicity in enhanced geothermal systems: From the coupled thermo-hydro-mechanical-chemical process to anthropogenic earthquake prediction. *Earth-Science Reviews*, *205*, 103182. https://doi.org/https://doi.org/10.1016/j.earscirev.2020.103182

Stichting Platform Geothermie. (2018). Master plan geothermal energy in the netherlands.

Van Wees, J., Buijze, L., Van Thienen-Visser, L., Nepveu, M., Wassing, B., Orlic, B., & Fokker, P. (2014). Geomechanics response and induced seismicity during gas field depletion in the netherlands. *Geothermics*, *52*, 206–219. https://doi.org/https://doi.org/10.1016/j.geothermics.2014.05.004

van Dinther, Y., Gerya, T. V., Dalguer, L. A., Mai, P. M., Morra, G., & Giardini, D. (2013). The seismic cycle at subduction thrusts: Insights from seismo-thermo-mechanical models. *Journal of Geophysical Research: Solid Earth*, *118*(12), 6183–6202. https://doi.org/https://doi.org/10.1002/2013JB010380

van Wees, J. D., Kahrobaei, S., Osinga, S., Wassing, B., Buijze, L., Candela, T., Fokker, P., ter Heege, J., & Vrijlandt, M. (2020). 3d models for stress changes and seismic hazard assessment in geothermal doublet systems in the netherlands. *Reykjavik, Iceland: World Geothermal Congresss*.

Yarushina, V., Podladchikov, Y., & Connolly, J. (2015). (de)compaction of porous viscoelastoplastic media: Solitary porosity waves. *Journal of Geophysical Research: Solid Earth*, *120*(7), 4843–4862. https://doi.org/10.1002/2014JB01126010.1093/gji/ggt199.

Appendix A

Preliminary tests

Preliminary tests were executed using the set up of the Petrini code (figure 3.1). The purpose of these experiments was to debug the code and to understand the influence of basic reservoir parameters: permeability and porosity. The material parameters that were used in the permeability experiments are listed in table A.1 and the material parameters used in the porosity experiments in table A.2 and the injection pressure rate used in both experiments was +100 Pa/s. Note that because these experiments were mainly used to debug the code, the corrections that are mentioned in section 3.6 are not yet implemented.

Figure A.1 shows that a higher reservoir permeability and a high reservoir porosity both result in less strain being accumulated within the well (figure A.1). This is because higher permeabilities and porosities allow the fluid to permeate from the well faster. This means that the fluid pressure is more evenly distributed throughout the well, resulting in less localized high strain rates (figure A.1).

TABLE A.1: Petrini code material parameters: permeability experiment

Parameters	Sticky Air	Reservoir	Units
Solid density (ρ^s)	1000	3000	$\frac{kg}{m^3}$
Shear viscosity of solid rock grains (η^0)	1e-3	1e21	$Pa \cdot s$
Porosity (φ)	1	1	%
Reference Porosity (φ_r)	1	1	%
Reference Permeability (k_r^{φ})	3e-16	1e-14 and 1e-18	m^2
Shear modulus of the solid rock grains (μ^0)	1e11	1e11	Pa
Compressive strength ($\sigma_{c,0}$)	3.0e6	3.0e6	Pa
Tensile strength ($\sigma_{t,0}$)	3.0e6	3.0e6	Pa
Internal friction coefficient (γ_{int})	0.3	0.3	-
Fluid density (ρ^f)	1000	1000	$\frac{kg}{m^3}$
Fluid bulk modulus	2.5e9	2.5e9	Pa
Fluid viscosity	1e-3	1e-3	$Pa \cdot s$

TABLE A.2: Petrini code material parameters: porosity experiment

Parameters	Sticky Air	Reservoir	Units
Solid density (ρ^s)	1000	3000	$\frac{kg}{m^3}$
Shear viscosity of solid rock grains (η^0)	1e-3	1e21	$Pa \cdot s$
Porosity (φ)	1	1 and 10	%
Reference Porosity (φ_r)	1	1	%
Reference Permeability (k_r^{φ})	3e-16	3e-17	m^2
Shear modulus of the solid rock grains (μ^0)	1e11	1e11	Pa
Compressive strength ($\sigma_{c,0}$)	3.0e6	3.0e6	Pa
Tensile strength ($\sigma_{t,0}$)	3.0e6	3.0e6	Pa
Internal friction coefficient (γ_{int})	0.3	0.3	-
Fluid density (ρ^f)	1000	1000	$\frac{kg}{m^3}$
Fluid bulk modulus	2.5e9	2.5e9	Pa
Fluid viscosity	1e-3	1e-3	$Pa \cdot s$

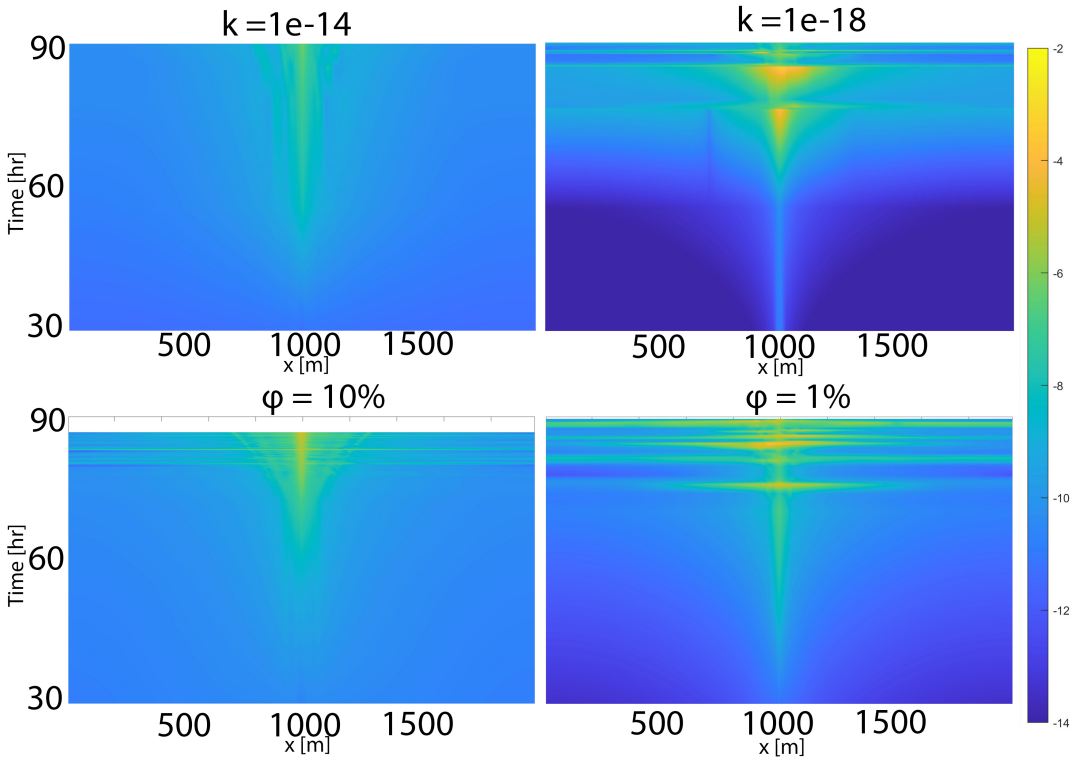

FIGURE A.1: Spatiotemporal evolution of the total strain rate during preliminary tests on the effect of the reservoir permeability and porosity. The well is located at the center of the x size, at 1000 m.

Appendix B

Parameter study results

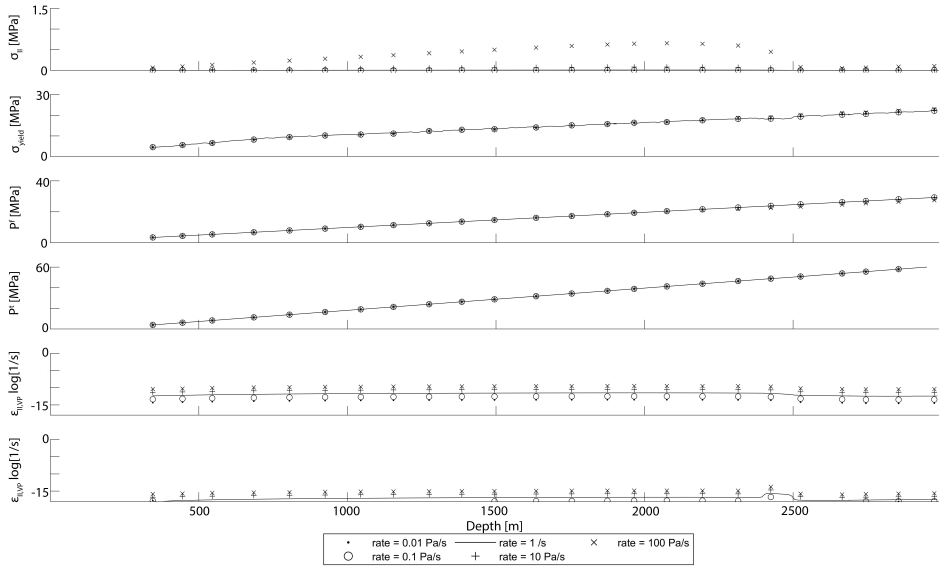

FIGURE B.1: Comparison between the pressure rate tests along the fault after 2 days of production. From top to bottom: 1) the second invariant of the stress tensor, 2) the yielding stress, 3) the fluid pressure, 4) the total pressure, 5) the second invariant of the strain rate tensor, 6) the second invariant of the visco-plastic strain rate tensor. Note that this comparison is made after 2 days of production, instead of 100 days for the other parameter studies. This is due to the fact that more time steps are necessary for the higher pressure rates.

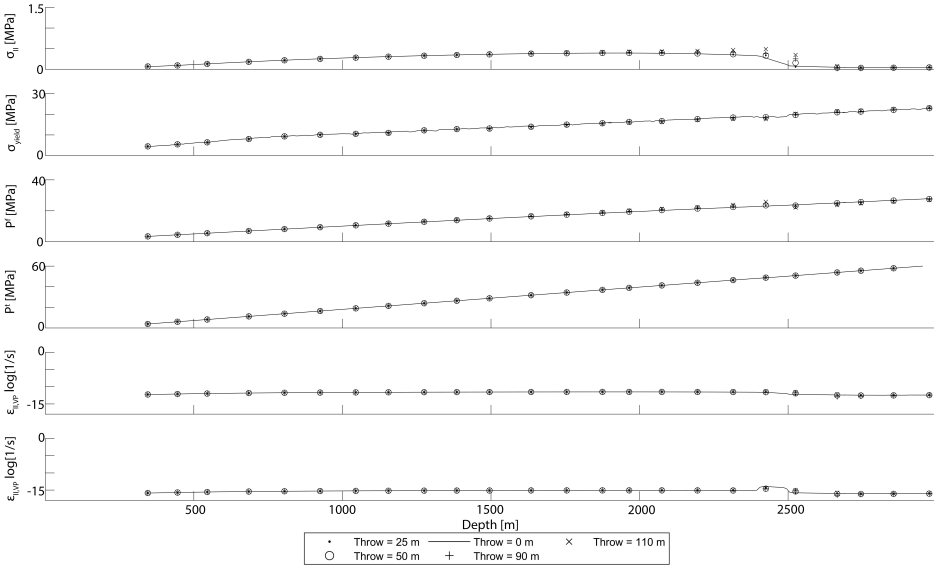

FIGURE B.2: Comparison between the fault throw tests along the fault after 100 days of production. From top to bottom: 1) the second invariant of the stress tensor, 2) the yielding stress, 3) the fluid pressure, 4) the total pressure, 5) the second invariant of the strain rate tensor, 6) the second invariant of the visco-plastic strain rate tensor.

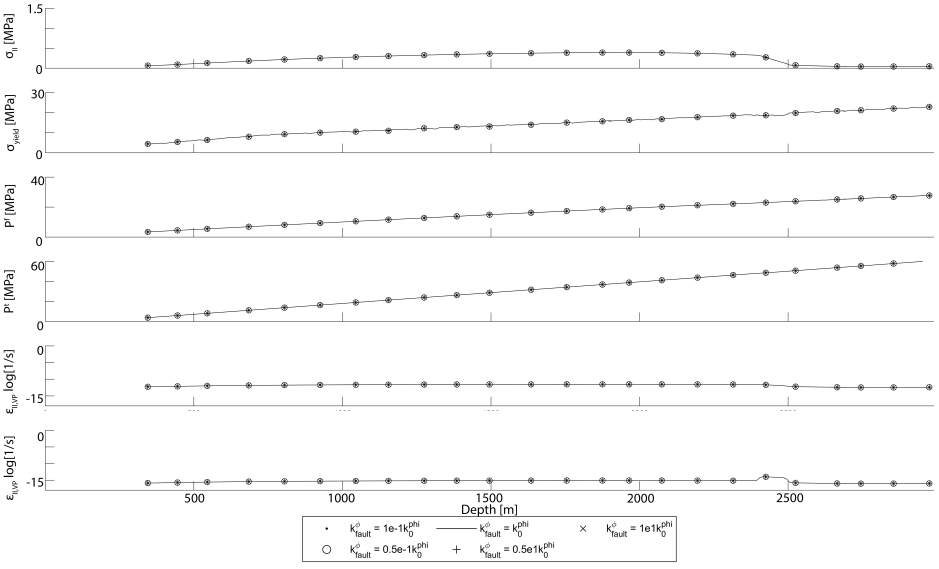

FIGURE B.3: Comparison between the fault permeability tests along the fault after 100 days of production. From top to bottom: 1) the second invariant of the stress tensor, 2) the yielding stress, 3) the fluid pressure, 4) the total pressure, 5) the second invariant of the strain rate tensor, 6) the second invariant of the visco-plastic strain rate tensor.

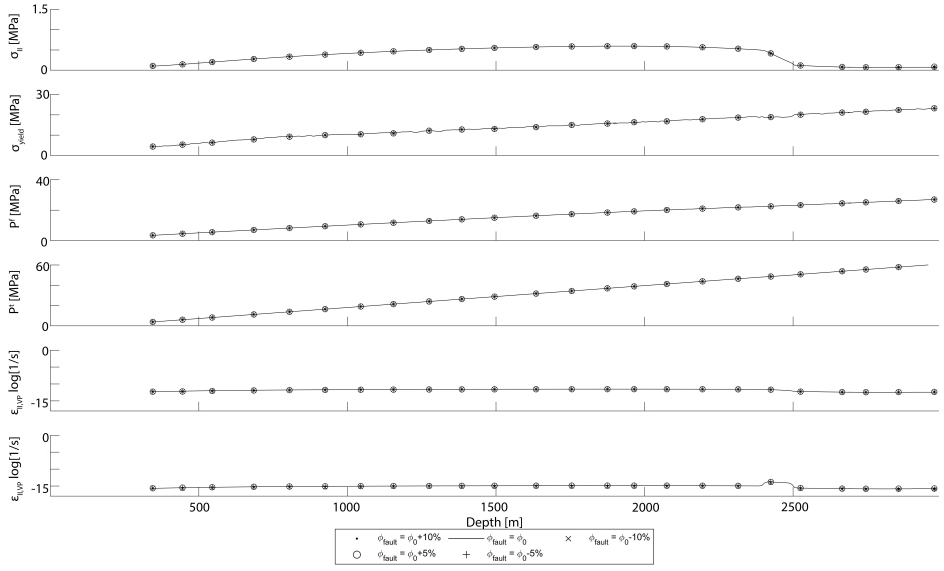

FIGURE B.4: Comparison between the fault porosity tests along the fault after 100 days of production. From top to bottom: 1) the second invariant of the stress tensor, 2) the yielding stress, 3) the fluid pressure, 4) the total pressure, 5) the second invariant of the strain rate tensor, 6) the second invariant of the visco-plastic strain rate tensor.

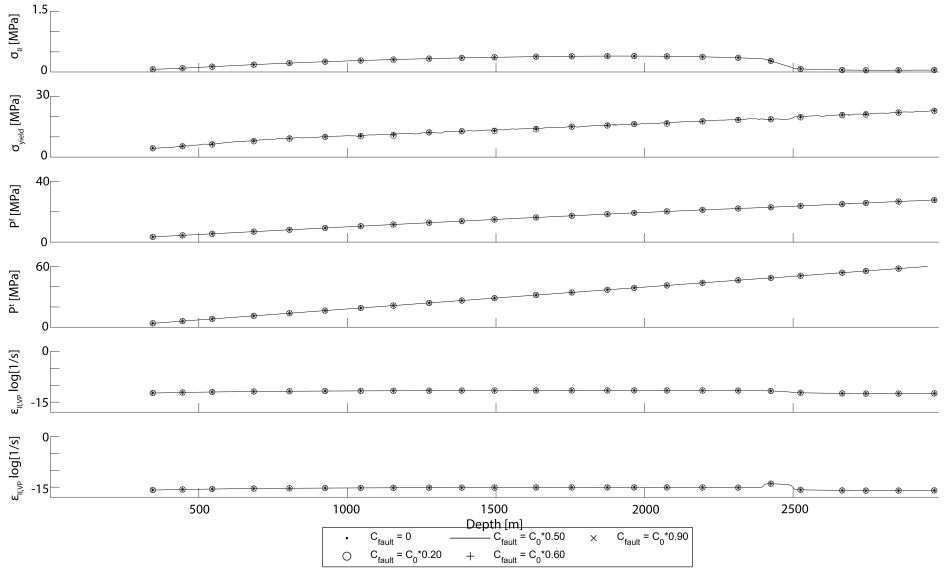

FIGURE B.5: Comparison between the fault strength tests along the fault after 100 days of production. From top to bottom: 1) the second invariant of the stress tensor, 2) the yielding stress, 3) the fluid pressure, 4) the total pressure, 5) the second invariant of the strain rate tensor, 6) the second invariant of the visco-plastic strain rate tensor.

Appendix C

Pressure rate test: deformation events

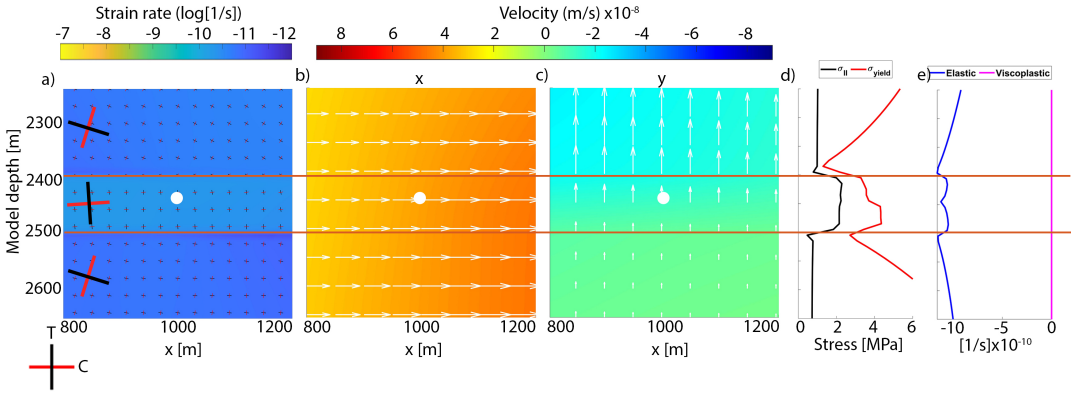

FIGURE C.1: The inter-seismic period of the event triggered by injecting fluid with a pressure rate of ± 10 Pa/s in and around the reservoir (top and bottom of reservoir are marked with red lines), the white dots signify the location of the injection well. The axes of maximum compressive stress (red) and maximum tensile stress (black) are horizontal and vertical respectively throughout the entire model. a) the total strain rate, b) the x component of the solid velocity, c) the y component of the solid velocity, d) the second invariant of the stress tensor (black) and the yielding stress (red) along the line x=$x_{injectionwell}$, d) the elastic (blue) and viscoplastic (magenta) (de)compaction rates along the line x=$x_{injectionwell}$.

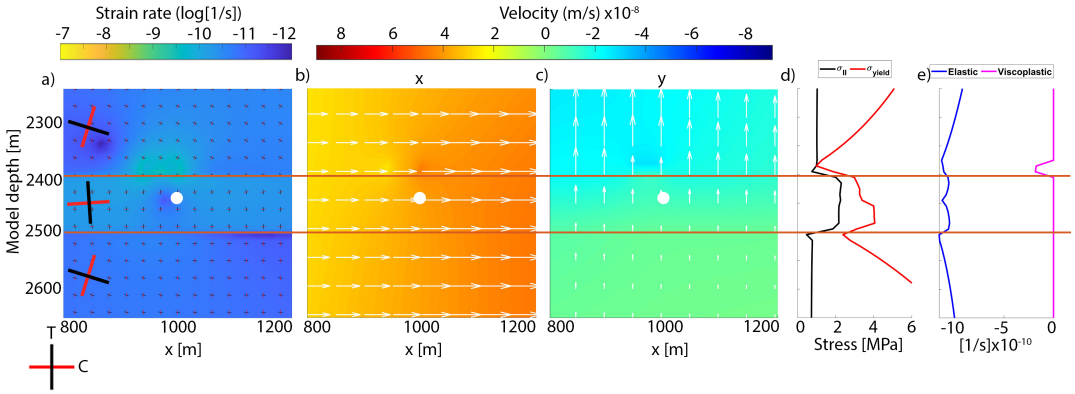

FIGURE C.2: The nucleation of the event triggered by injecting fluid with a pressure rate of ± 10 Pa/sin and around the reservoir (top and bottom of reservoir are marked with red lines), the white dots signify the location of the injection well. The axes of maximum compressive stress (red) and maximum tensile stress (black) are horizontal and vertical respectively throughout the entire model. a) the total strain rate, b) the x component of the solid velocity, c) the y component of the solid velocity, d) the second invariant of the stress tensor (black) and the yielding stress (red) along the line x=$x_{injectionwell}$, d) the elastic (blue) and viscoplastic (magenta) (de)compaction rates along the line x=$x_{injectionwell}$.

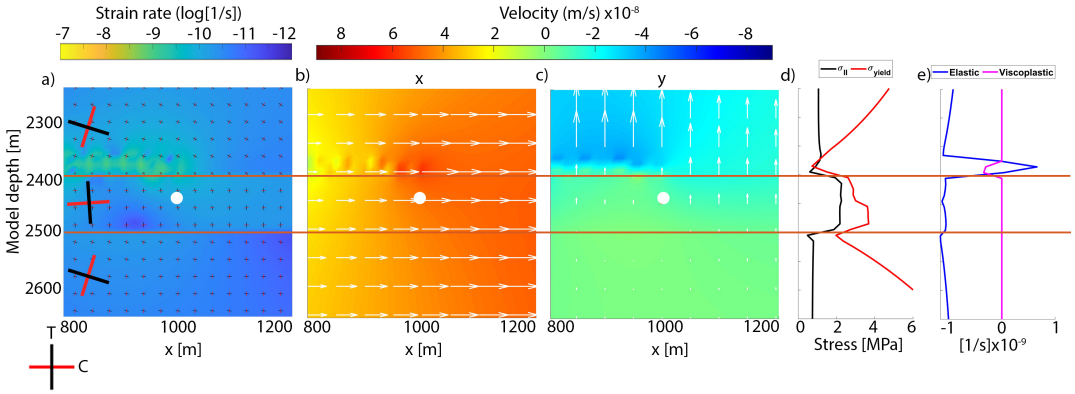

FIGURE C.3: The propagation of the event triggered by injecting fluid with a pressure rate of ± 10 Pa/sin and around the reservoir (top and bottom of reservoir are marked with red lines), the white dots signify the location of the injection well. The axes of maximum compressive stress (red) and maximum tensile stress (black) are horizontal and vertical respectively throughout the entire model. a) the total strain rate, b) the x component of the solid velocity, c) the y component of the solid velocity, d) the second invariant of the stress tensor (black) and the yielding stress (red) along the line x=$x_{injectionwell}$, d) the elastic (blue) and viscoplastic (magenta) (de)compaction rates along the line x=$x_{injectionwell}$.

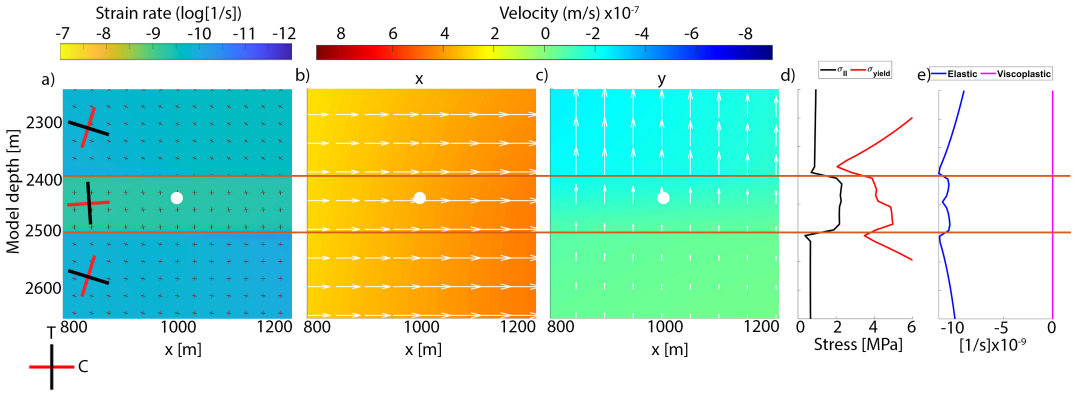

FIGURE C.4: The inter-seismic period of the event triggered by injecting fluid with a pressure rate of ± 100 Pa/sin and around the reservoir (top and bottom of reservoir are marked with red lines), the white dots signify the location of the injection well. The axes of maximum compressive stress (red) and maximum tensile stress (black) are horizontal and vertical respectively throughout the entire model. a) the total strain rate, b) the x component of the solid velocity, c) the y component of the solid velocity, d) the second invariant of the stress tensor (black) and the yielding stress (red) along the line x=$x_{injectionwell}$, d) the elastic (blue) and viscoplastic (magenta) (de)compaction rates along the line x=$x_{injectionwell}$.

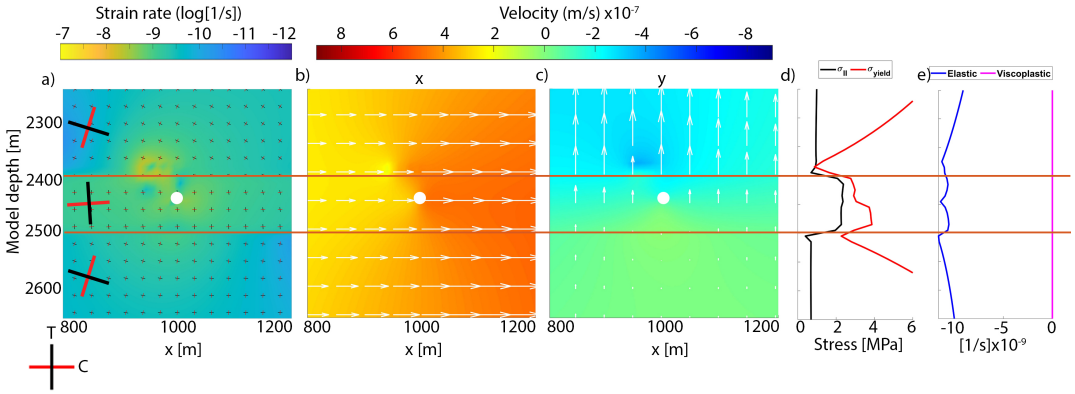

FIGURE C.5: The nucleation of the event triggered by injecting fluid with a pressure rate of ± 100 Pa/sin and around the reservoir (top and bottom of reservoir are marked with red lines), the white dots signify the location of the injection well. The axes of maximum compressive stress (red) and maximum tensile stress (black) are horizontal and vertical respectively throughout the entire model. a) the total strain rate, b) the x component of the solid velocity, c) the y component of the solid velocity, d) the second invariant of the stress tensor (black) and the yielding stress (red) along the line x=$x_{injectionwell}$, d) the elastic (blue) and viscoplastic (magenta) (de)compaction rates along the line x=$x_{injectionwell}$.

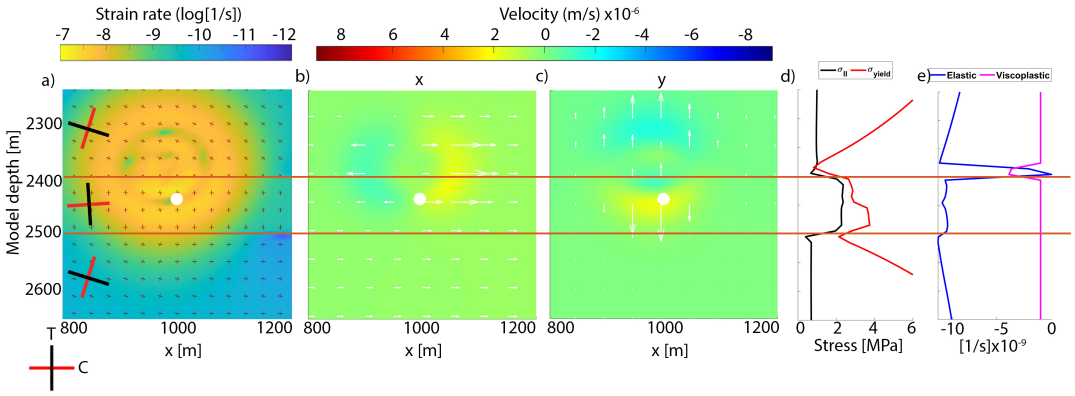

FIGURE C.6: The propagation of the event triggered by injecting fluid with a pressure rate of ± 100 Pa/sin and around the reservoir (top and bottom of reservoir are marked with red lines), the white dots signify the location of the injection well. The axes of maximum compressive stress (red) and maximum tensile stress (black) are horizontal and vertical respectively throughout the entire model. a) the total strain rate, b) the x component of the solid velocity, c) the y component of the solid velocity, d) the second invariant of the stress tensor (black) and the yielding stress (red) along the line x=$x_{injectionwell}$, d) the elastic (blue) and viscoplastic (magenta) (de)compaction rates along the line x=$x_{injectionwell}$.